

UC Berkeley

UC Berkeley Previously Published Works

Title

Optimal design of vascular stents using a network of 1D slender curved rods

Permalink

<https://escholarship.org/uc/item/8f28b8s0>

Authors

Čanić, Sunčica
Grubišić, Luka
Lacmanović, Domagoj
et al.

Publication Date

2022-05-01

DOI

10.1016/j.cma.2022.114853

Peer reviewed

MATHEMATICAL AND COMPUTATIONAL MODELING OF POROELASTIC CELL SCAFFOLDS USED IN THE DESIGN OF AN IMPLANTABLE BIOARTIFICIAL PANCREAS.

YIFAN WANG*, SUNČICA ČANIĆ†, MARTINA BUKAČ‡, CHARLES BLAHA§, AND SHUVO ROY¶

Abstract. We present a multi-scale mathematical model and a novel numerical solver to study blood plasma flow and oxygen concentration in a prototype model of an implantable Bioartificial Pancreas (iBAP) that operates under arteriovenous pressure differential without the need for immunosuppressive therapy. The iBAP design consists of a poroelastic cell scaffold containing the healthy transplanted cells, encapsulated between two semi-permeable nano-pore size membranes to prevent the patient's own immune cells from attacking the transplant. The device is connected to the patient's vascular system via an anastomosis graft bringing oxygen and nutrients to the transplanted cells of which oxygen is the limiting factor for long-term viability. Mathematically, we propose a (nonlinear) fluid-poroelastic structure interaction model to describe the flow of blood plasma through the scaffold containing the cells, and a set of (nonlinear) advection-reaction-diffusion equations defined on moving domains to study oxygen supply to the cells. These macro-scale models are solved using finite element method based solvers. One of the novelties of this work is the design of a novel second-order accurate fluid-poroelastic structure interaction solver, for which we prove that it is unconditionally stable. At the micro/nano-scale, Smoothed Particle Hydrodynamics (SPH) simulations are used to capture the micro/nano-structure (architecture) of cell scaffolds and obtain macro-scale parameters, such as hydraulic conductivity/permeability, from the micro-scale scaffold-specific architecture. To avoid expensive micro-scale simulations based on SPH simulations for every new scaffold architecture, we use Encoder-Decoder Convolution Neural Networks. Based on our numerical simulations, we propose improvements in the current prototype design. For example, we show that highly elastic scaffolds have a higher capacity for oxygen transfer, which is an important finding considering that scaffold elasticity can be controlled during their fabrication, and that elastic scaffolds improve cell viability.

The mathematical and computational approaches developed in this work provide a benchmark tool for computational analysis of not only iBAP, but also, more generally, of cell encapsulation strategies used in the design of devices for cell therapy and bio-artificial organs.

1. Introduction. We present a mathematical model and a numerical solver to study a design of an implantable bioartificial pancreas (iBAP) that operates without the need for immunosuppressive drugs. The main purpose of a bioartificial pancreas is to treat Type 1 Diabetes (T1D), which is an autoimmune disease that affects over 1.6 million people in the United States. The current standard of care is glucose monitoring coupled with exogenous insulin administration via injections or pump. Less common interventions, such as transplantation of islets (spheroid-like cell aggregates that contain endocrine cells of the pancreas) or pancreas transplantation, are reserved for those patients for whom insulin therapy does not allow adequate metabolic control and who experience severe hypoglycemic events. The main obstacles for islet transplantation are poor graft function within a few years post transplantation, negative side effects of lifelong immunosuppression, and pancreas donor shortage. A bioartificial pancreas promises to expand islet cell therapy to substantially more T1D patients because of its immunoprotective cell encapsulation design, and because the types of cells that can be used in its design include not only the pancreatic islets but also those derived from human pluripotent stem cells. The human pluripotent stem cells can be used to create mature β -cells found in pancreatic islets, which are responsible for insulin production [37]. This promises solution to the shortage of donor organs as a source of pancreatic islets, while cell encapsulation eliminates the need for immunosuppressants.

A prototype of the bioartificial pancreas, under development in Dr. Roy's Lab [27, 22, 38, 28],

*Department of Mathematics, University of California, Irvine (qcutexu@gmail.com).

†Department of Mathematics, University of California, Berkeley (canics@berkeley.edu).

‡Department of Applied and Computational Mathematics and Statistics, University of Notre Dame (mbukac@nd.edu).

§University of California, San Francisco (blahac@gmail.com).

¶University of California, San Francisco (Shuvo.Roy@ucsf.edu).

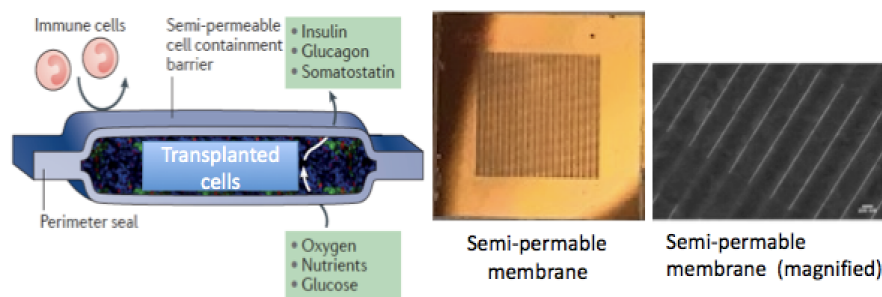


FIG. 1. Left: An illustration of an islet encapsulation device [18]; Middle: Semi-permeable silicon membrane; Right: A scanning electron microscope (SEM) image of the membrane surface illustrating slits $2\mu\text{m}$ in length and 7nm in width (courtesy of Dr. Roy).

46 consists of a biocompatible hydrogel scaffold containing the transplanted cells, encapsulated
 47 between two semi-permeable nanopore silicon membranes. See Fig. 1. The silicon membranes
 48 are specifically designed for immunoprotection of the encapsulated islets, while enabling high
 49 oxygen delivery and high mass transfer rates of glucose and insulin. They protect the transplant
 50 from being attacked by the patient's immune system (antibodies and cytokines), while allowing
 51 passage of oxygen and nutrients necessary for long-term viability of the organ. The membranes
 52 are surface-modified with polyethylene glycol (PEG) to inhibit protein adsorption, fouling, and
 53 thrombosis [22].

54 The encapsulated cell chamber is connected to anastomosis grafts, which connect the device
 55 to the patient's vascular system. See Fig. 2. One anastomosis graft brings oxygen and nutrients
 56 rich blood to the cell chamber, while the other transports away the insulin produced by the cells.
 57 The anastomosis grafts are connected to an artery on one side, and a vein on the other, thereby
 58 generating sufficient pressure gradient for significant flow within the anastomosis graft. See the
 59 sketch in Fig. 2, which shows the device implanted in a patient's arm and connected to the radial
 60 artery on one end, and a vein on the other.

61 One of the key challenges in bioartificial pancreas design is sufficient oxygen supply to the
 transplanted cells within the hydrogel scaffold. To increase oxygen concentration in the cell

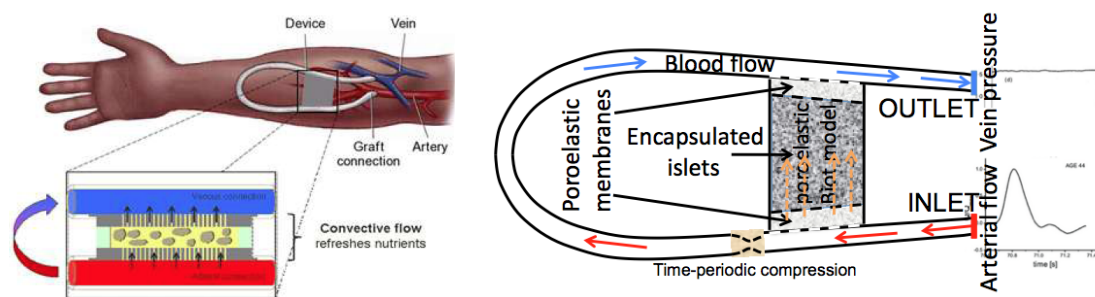


FIG. 2. Left: An illustration of the implantable intravascular bioartificial pancreas device in the arm of a T1D patient (from [38]). Right: A sketch showing the graft and the encapsulation chamber consisting of two poroelastic membranes and the islet chamber in the middle. The figure also includes our suggestion for the placement of a time-periodic compression device downstream from the chamber, to increase convective flow into the chamber and flush out albumin deposits near the membrane observed in steady flow.

62

63 chamber (poroelastic hydrogel), ultrafiltrate channels are drilled within the hydrogel for advection

enhanced oxygen supply. See Fig. 3.

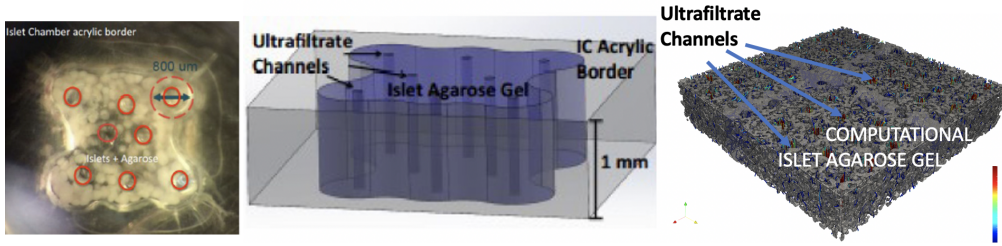


FIG. 3. Ultrafiltrate channels in agarose gel.

64
65

In this manuscript we study the design and performance of a second generation implantable Bioartificial Pancreas prototype. A sketch of the prototype device is shown in Fig. 4. This figure

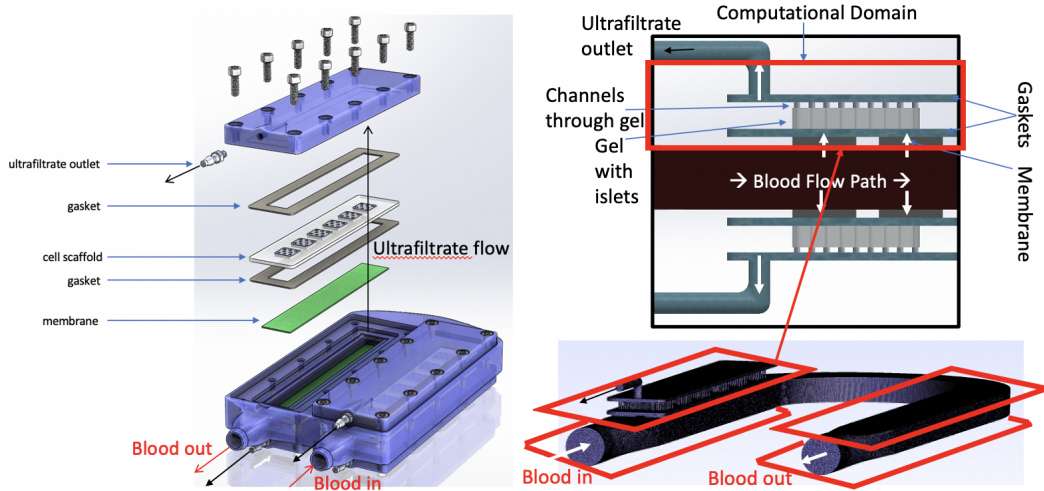


FIG. 4. A prototype of a implantable Bioartificial Pancreas Device. The red boxes on the bottom right figure show the location where the four islet chambers are located. Only one of the four chambers is fully depicted in Fig. 4 bottom right. A more detailed, magnified sketch of two such chambers is shown on the top figure on the right. The top chamber in the red rectangle shows the computational domain.

66

67 shows the device with the inflow-outflow channel, and four islet chambers, two on either side of
68 the channel. The inlet to the channel is connected via an anastomosis graft to an artery, and the
69 outlet to a vein. See Fig. 5, which shows a prototype implantable Bioartificial Pancreas (iBAP)
70 implanted into a porcine model. A pressure drop between an artery and a vein drives the blood
71 flow through the channel. Each of the four islet chambers is connected to the blood-supplying
72 channel through a number of semipermeable silicon membranes. The nutrients rich blood flow
73 gets filtered through the membranes and the filtered blood plasma further flows through a gasket
74 and into a hydrogel containing the transplanted cells. As the nutrients rich blood plasma passes
75 through the hydrogel, it feeds the pancreatic islets, and it picks up the produced insulin, which
76 is then carried away from the hydrogel through a gasket with an attached outlet (ultrafiltrate
77 outlet; see Fig. 4). The four ultrafiltrate outlets (each associated with one islet chamber)
78 are connected via a catheter to a vein, which receives insulin rich blood plasma.

79 Islet chamber details as used in the design of the computational domain, are presented in the
80 sketch shown in Fig. 6. The blood channel supplying oxygen and nutrients rich blood to the islet

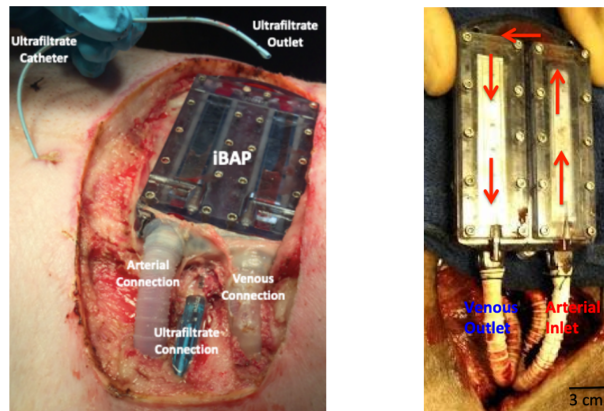


FIG. 5. A prototype of an implantable Bioartificial Pancreas (iBAP) implanted into a porcine model.

81 chamber is not shown in Fig. 6. The four membranes are shown in Fig. 6 at the bottom of the
 82 sketch with the “inlet” arrows pointing in the flow direction. Two (rectangular) membranes are
 83 in the front, and two in the back. The thin gasket region containing the oxygen and nutrients rich
 84 blood plasma is adjacent to the islet chamber (poroelastic medium containing the cells), shown
 85 in orange color. Fig. 6 also shows ultrafiltrate channels in orange color, distributed throughout
 86 the islet chamber. The ultrafiltrate flow that passes through the cell chamber enters the top
 87 gasket region which collects the insulin rich blood plasma. The insulin rich blood plasma exits
 88 the gasket through an ultrafiltrate outlet and enters the “returning” part of the anastomosis graft
 (not shown in this sketch) connected to the patient’s vein.

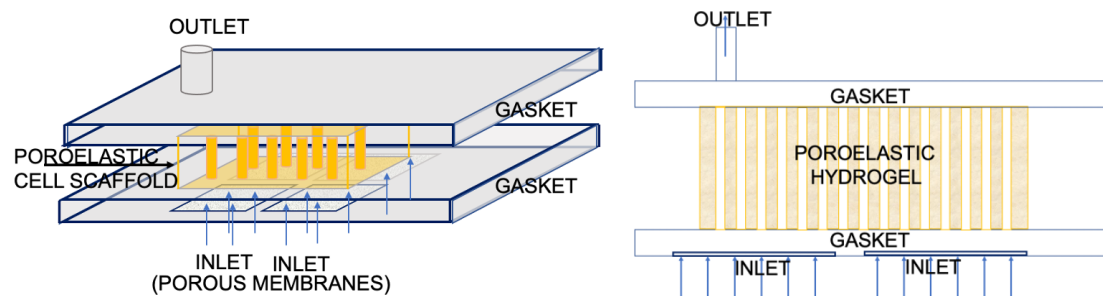


FIG. 6. Left: A 3D sketch of the prototype device (computational domain) showing the inlet through four semi-permeable membranes (four blue squares at the bottom), the hydrogel chamber (in orange); ultrafiltrate channels in hydrogel chamber (orange cylinders), and two gaskets – one at the bottom and one at the top of the hydrogel chamber. The anastomosis graft connected to the inlet and outlet is not shown. Right: A 2D slice through the 3D device shown on the left.

89

90 The main goal of this manuscript is to design a multi-scale mathematical model and a
 91 computational software to study fluid flow (blood plasma) and oxygen concentration within the
 92 bioartificial pancreas, which can be used to study the performance of the current design and
 93 suggest improvements in terms of increased oxygen supply to the transplanted cells. The key
 94 mathematical goals are: (1) To capture the interaction between blood plasma (a Newtonian
 95 viscous, incompressible fluid) and a poroelastic medium (cell scaffold), which is a hydrogel in
 96 which the permeability properties depend on the fluid content [19], thereby giving rise to a

97 **nonlinear** mathematical model, (2) To capture oxygen concentration in the cell chamber and
 98 the gasket. In both of these goals it is important to capture the micro-structure of the hydrogel,
 99 which calls for multi-scale modeling.

100 As we shall see below, elasticity of cell scaffolds is important in studying filtrate flow and
 101 oxygen concentration in cell scaffolds. This is especially important since elasticity can be con-
 102 trolled in the fabrication of agarose hydrogel scaffolds, fabricated using the approaches presented
 103 in [37]. Mathematically, devising a higher-order accurate fluid-structure interaction computa-
 104 tional solver capturing **poroelasticity** of the scaffolds in which permeability depends on the fluid
 105 content is highly nontrivial. In this manuscript we design such a solver and prove, using rigorous
 106 stability estimates, that the resulting numerical solver for a corresponding linearized problem is
 107 unconditionally stable. This is one of the mathematical novelties of this work.

108 More specifically, in this manuscript we present a multi-scale model consisting of the fol-
 109 lowing. At the **macro scale**, we consider the following partial differential equations (PDE)
 110 models:

- 111 1. A fluid-structure interaction (FSI) model describing the interaction between the blood
 112 plasma modeled by the Navier-Stokes or time-dependent Stokes equations for an incom-
 113 pressible, viscous fluid, and a poroelastic hydrogel containing the cells, modeled by the
 114 nonlinear Biot equations (see Sec. 2.1). The nonlinearity in the Biot equations comes
 115 from the dependence of the hydrogel’s permeability on fluid content/porosity [19];
- 116 2. Two advection-reaction-diffusion models describing oxygen concentration within the
 117 poroelastic hydrogel containing the cells, and oxygen concentration within the gasket
 118 containing blood plasma (see Sec. 2.2). The two models are coupled to the FSI model
 119 above through the fluid advection velocity, and through the information about the do-
 120 main motion. Additionally, the two advection-reaction-diffusion models are coupled
 121 among themselves across the interface $\Gamma(t)$ separating the gasket region from the poro-
 122 elastic hydrogel scaffold. The coupling conditions describe oxygen transfer from the gasket
 123 region to the poroelastic scaffold.

124 The FSI model and the advection-reaction-diffusion models are solved using Finite-Element
 125 Method based numerical solvers. Of particular interest is a second-order accurate fluid-poroelastic
 126 structure interaction solver that we introduce in this manuscript, and for which we prove that it is
 127 unconditionally stable for the FSI problem with linearized interface motion (fixed fluid domain).
 128 This is presented in Sec. 3.1.

129 At the **micro scale**, a particle-based Smoothed Particle Hydrodynamics (SPH) model is
 130 used to simulate the micro-scale 3D poroelastic structures of hydrogels and calculate the local
 131 hydraulic conductivity for every “control” sub-volume of the 3D poroelastic hydrogel. This
 132 information is then used to **couple the micro and macro-scale** simulations by obtaining the
 133 3D macro-scale permeability tensor κ from the local fluid content obtained from the micro-scale
 134 SPH simulations. See Sec. 2.1.

135 To avoid the time-consuming and computationally expensive SPH simulations for every new
 136 hydrogel structure, we use Encoder-Decoder Convolution Neural Networks, trained on a set of
 137 our synthetic data (calculated off-line), to obtain κ for new hydrogel structures which are either
 138 generated synthetically, or for the actual hydrogel structures that can be imaged using high
 139 precision laser scanning confocal microscopy.

140 Micro- and macro-scale coupling is also used at the **inlet**, where we impose macro-scale inlet
 141 flow data, see (2.16) below, obtained from the pressure data in the anastomosis graft coupled
 142 with the **micro-scale** membrane parameters such as the membrane thickness, pore size, etc.
 143 using a Darcy-type relationship (2.15) derived from experiments with the actual silicon nanopore
 144 size membranes considered in this study [22].

145 Finally, we use our mathematical models and numerical solvers to simulate filtration flow
 146 and oxygen concentration for a prototype Bioartificial Pancreas, shown in Figs. 4 and 6. The

147 results of our numerical simulation are presented in Sec. 4. Based on the simulations we propose
 148 improvements in the design of the implantable Bioartificial Pancreas, which are discussed in
 149 Sections 4 and 5.

150 Conclusions are presented in Sec. 5.

151 To the best of our knowledge, this is the first multi-scale, 3D mathematical and computational
 152 model of a bioartificial pancreas, which captures plasma flow interacting with a cell-seeded scaffold
 153 and oxygen concentration within the pancreas. Previous models usually address “subsets” of
 154 the bioartificial pancreas design, such as, e.g., oxygen concentration and insulin secretion by
 155 pancreatic islets. In particular, we mention here an excellent study by Buchwald [7] that informed
 156 our own work in terms of advection-reaction-diffusion models for oxygen concentration, where
 157 an advection-reaction-diffusion model and the parameters were provided. These parameters and
 158 a simplified oxygen concentration and consumption computational model was recently utilized
 159 in a study of a simplified bioartificial pancreas without membrane encapsulation, consisting of
 160 an acellular tubular graft “lined” with pancreatic islets coated on the outer surface using a
 161 hydrogel carrier [23]. In a similar set-up, the work in [21] investigated an *in vitro* cylindrical
 162 perfusion system to study oxygen effects on islet-like clusters immobilized in alginate hydrogel.
 163 No computational model for the set up was presented in this work.

164 The next step of the model development for bioartificial pancreas is modeling glucose-stimulated
 165 insulin secretion by the β -cells of pancreatic islets. In [9, 10] Buchwald et al. developed a math-
 166 ematical model and a Finite Element Method solver to study insulin secretion in avascular pan-
 167 creatic islets that can be used to calculate insulin secretion for arbitrary geometries of cultured,
 168 perfused, transplanted, or encapsulated islets in response to various glucose profiles. The model
 169 was further used in [11] to study dynamic perfusion with isolated human islets.

170 However, none of the previous models considered the complexity of an artificial pancreas
 171 design such as the one presented in this paper. One of the main novelties of this paper is the
 172 fluid-structure interaction model that simulates blood plasma filtration through a poroelastic
 173 cell scaffold, which is then coupled to an oxygen concentration model, and in a further study,
 174 to an insulin secretion model. This has not been done before in the context of a bioartificial
 175 pancreas design. Including poroelasticity, as we do in this work, is crucial for manufacturing cell
 176 scaffolds with “optimal” elasticity properties for long term cell viability. More information about
 177 fluid-poroelastic structure interaction can be found in [3, 40, 36, 2, 35, 6, 45, 15, 44]. None of
 178 those models, however, were studied in the context of a bioartificial pancreas design.

179 We remark that the mathematical and computational approaches presented in this work can
 180 be used not only for the design of a bioartificial pancreas presented here, but also, more generally,
 181 for the analysis of encapsulation strategies used in the design of devices for cell therapy and bio-
 182 artificial organs [39].

183 **2. The macro-scale mathematical models.** We present two sets of models: one describ-
 184 ing the flow of blood plasma in the gasket and in the poroelastic scaffold, presented in Sec. 2.1,
 185 and the other describing concentration of oxygen in the gasket and in the poroelastic scaffold,
 186 presented in Sec. 2.2 below. The equations for oxygen concentration are coupled to the fluid flow
 187 model via advection velocity and the fluid domain motion, namely, the equations for oxygen con-
 188 centration in the gasket and in the hydrogel are solved on *moving domains*. As we show below,
 189 including hydrogel elasticity and simulations on moving domains is significant for the analysis of
 190 oxygen concentration in highly elastic hydrogels.

191 We start by presenting details of the fluid-structure interaction (FSI) model describing the
 192 blood plasma flow through the gasket and poroelastic hydrogel.

193 **2.1. A fluid-structure interaction model for blood plasma and poroelastic scaf-**
 194 **fold.** As mentioned earlier, blood plasma enters the islet chamber through four nano-pore size
 195 membranes. See Fig. 6. The membranes are located at the inlet of the gasket region containing

196 the blood plasma. We will use $\Omega_f(t)$ to denote the fluid filled gasket region, and Γ_{in} to denote
 197 the part of the boundary of $\Omega_f(t)$ corresponding to the inlet. The dependence on t of $\Omega_f(t)$
 198 denotes the fact that the fluid domain changes as a function of time due to the interaction be-
 199 tween the fluid flow and the poroelastic scaffold sitting on top of $\Omega_f(t)$. The reference (fixed)
 200 configuration of the fluid domain will be denoted by $\hat{\Omega}_f$. The poroelastic scaffold region/domain,
 201 which is adjacent to $\Omega_f(t)$ will be denoted by $\Omega_p(t)$, and its reference configuration by $\hat{\Omega}_p$. Even
 202 though the poroelastic scaffold region is moving, the equations are typically written on a fixed,
 203 reference domain $\hat{\Omega}_p$. We denote by $\Gamma(t)$ the moving interface separating the gasket region from
 204 the poroelastic scaffold region, with its reference configuration denoted by $\hat{\Gamma}$.

205 In the case when poroelastic scaffold contains ultrafiltrate channels, the fluid domain is
 206 extended to the channels as well. In this case the boundary between the channels and the
 207 poroelastic scaffold is also assumed elastic, and is a part of the fluid domain boundary $\Gamma(t)$. See
 208 Fig. 7 below.

209 **The fluid model.** To model the flow of blood plasma in the gaskets (and in the ultrafiltrate
 210 channels) as shown in Fig. 6, we use the Navier-Stokes equations for an incompressible, viscous,
 211 Newtonian fluid. Since the Reynolds number in the gasket flow is relatively small, the time-
 212 dependent Stokes equations are also adequate. The Navier-Stokes equations defined on $\Omega_f(t)$ are
 213 given by:

$$214 \quad (2.1) \quad \left. \begin{aligned} \rho_f \left(\frac{\partial \mathbf{u}_f}{\partial t} + (\mathbf{u}_f \cdot \nabla) \mathbf{u}_f \right) &= \nabla \cdot \boldsymbol{\sigma}_f(\mathbf{u}_f, p_f) + \mathbf{F}_f, \\ \nabla \cdot \mathbf{u}_f &= 0, \end{aligned} \right\} \text{in } \Omega_f(t) \times (0, T),$$

215 where \mathbf{u}_f is the fluid velocity, $\boldsymbol{\sigma}_f = -p_f \mathbf{I} + 2\mu_f \mathbf{D}(\mathbf{u}_f)$ is the Cauchy stress tensor modeling
 216 Newtonian fluid, p_f stands for the fluid pressure, $\mathbf{D}(\mathbf{u}_f) = (\nabla \mathbf{u}_f + (\nabla \mathbf{u}_f)^T)/2$ stands for the
 217 symmetrized velocity gradient, μ_f is the fluid viscosity, ρ_f is the fluid density, and \mathbf{F}_f denotes
 218 the external force term. To close the problem, initial and boundary conditions will be specified
 219 in Section 2.1.

220 **The poroelastic structure model (cell scaffold).** To model the poroelastic cell scaffold
 221 i.e., the poroelastic structure, we use Biot's equations of poroelasticity, given by

$$222 \quad (2.2) \quad \left. \begin{aligned} \rho_p \frac{\partial^2 \boldsymbol{\eta}}{\partial t^2} &= \nabla \cdot \boldsymbol{\sigma}_p(\boldsymbol{\eta}, p_p) + \mathbf{F}^s, \\ \frac{\partial}{\partial t} (c_0 p_p + \alpha \nabla \cdot \boldsymbol{\eta}) &= \nabla \cdot (\boldsymbol{\kappa} \nabla p_p) + F_p, \\ \mathbf{u}_p &= -\boldsymbol{\kappa} \nabla p_p, \end{aligned} \right\} \text{in } \hat{\Omega}_p \times (0, T).$$

223 The model is given in terms of displacement $\boldsymbol{\eta}$ of the poroelastic matrix from its reference
 224 configuration $\hat{\Omega}_p$, and the fluid pore pressure p_p in the Lagrangian framework, with filtration
 225 velocity, \mathbf{u}_p , given in terms of the fluid pore pressure gradient via Darcy's law (third equation in
 226 (2.2)). We note that \mathbf{u}_p is the *relative* filtration velocity with respect to the poroelastic scaffold
 227 motion. The density of the solid material is denoted by ρ_p , $\boldsymbol{\kappa}$ is the hydraulic conductivity
 228 tensor, and \mathbf{F}^s and F_p are external force and source term, respectively. Coefficient c_0 is the
 229 storage coefficient, α is the Biot-Willis parameter accounting for the coupling strength between
 230 the fluid and the solid, and $\boldsymbol{\sigma}_p$ is the stress tensor of the poroelastic medium, which is given
 231 by $\boldsymbol{\sigma}_p = \boldsymbol{\sigma}_E - \alpha p_p \mathbf{I}$, where $\boldsymbol{\sigma}_E$ denotes the elasticity stress tensor and \mathbf{I} is the identity matrix.
 232 To close the system, a constitutive law for $\boldsymbol{\sigma}_E(\boldsymbol{\eta})$ describing the elastic material properties
 233 needs to be specified. Here, we assume the linear Saint Venant-Kichhoff material, given by
 234 $\boldsymbol{\sigma}_E = 2\mu_S \mathbf{D}(\boldsymbol{\eta}) + \lambda_S \nabla \cdot \boldsymbol{\eta} \mathbf{I}$, where μ_S and λ_S are Lamé constants. The corresponding initial and
 235 boundary conditions will be specified in Section 2.1.

236 Biot equations have been used to model hydrogel scaffolds by many authors, see e.g., [46, 19,
 237 16]. In particular, it was noted that hydrogel's permeability depends on the fluid content, which
 238 is defined as an increment in the volumetric fraction of the fluid component Φ with respect to
 239 its reference value Φ_0 :

$$240 \quad (2.3) \quad \zeta = \Phi - \Phi_0, \text{ where } \Phi = \frac{V_f(x, y, z, t)}{V(x, y, z, t)}.$$

241 Here $V_f(x, y, z, t)$ is the fluid volume and $V(x, y, z, t)$ is the representative elementary volume
 242 centered at (x, y, z) at time t . The quantity Φ is also referred to as porosity, and Φ_0 is the
 243 equilibrium porosity.

One can show that ζ defined above can be expressed in terms of the fluid pressure and the volumetric change of pores' volume as

$$\zeta = c_0 p_p + \alpha \nabla \cdot \boldsymbol{\eta},$$

244 which is the quantity appearing under the time derivative in the second equation in (2.2). The
 245 dependence of hydrogel's permeability on ζ was noted in e.g., [19, 24], and it is associated with
 246 swelling of hydrogels. To describe the dependence of $\boldsymbol{\kappa}$ on ζ , it is common to use the Kozeny-
 247 Carman equation:

$$248 \quad (2.4) \quad \boldsymbol{\kappa}(x, y, z, \Phi) = \boldsymbol{\kappa}_0(x, y, z) \left(\frac{1 - \Phi_0}{1 - \Phi} \right)^\beta.$$

249 Here the exponent β was calculated for hydrogels to be $\beta = 2/3$ using geometric considera-
 250 tions, see [19]. The factor $\boldsymbol{\kappa}_0$ is the reference, equilibrium permeability. In our simulations,
 251 $\boldsymbol{\kappa}_0 = \boldsymbol{\kappa}_0(x, y, z)$ will be estimated from the micro-scale simulations using Smoothed Particle
 252 Hydrodynamics and Encoder-Decoder Convolution Neural Networks. See Sec. 3.3. Throughout
 253 this manuscript, we will be using either a given permeability $\boldsymbol{\kappa}(x, y, z, t)$, or a nonlinear perme-
 254 ability $\boldsymbol{\kappa} = \boldsymbol{\kappa}(x, y, z, \Phi) = \boldsymbol{\kappa}(\zeta)$ given by (2.4), rendering the Biot system (2.2) a *nonlinear* Biot
 255 problem.

256 **Moving domain and ALE formulation.** Before we describe the coupling conditions
 257 between the fluid and poroelastic structure, we must deal with the fact that the fluid domain
 258 is moving, and the fluid equations are written in the Eulerian framework on $\Omega_f(t)$, while the
 259 structure equations, i.e., the Biot model, is given in the Lagrangian framework on the reference
 260 domain $\hat{\Omega}_p$. To deal with the motion of the fluid domain, we introduce a family of Arbitrary
 261 Lagrangian-Eulerian (ALE) mappings that map the reference fluid domain $\hat{\Omega}_f$ onto the current
 262 domain $\Omega(t)$, and rewrite the fluid equations in the so-called ALE form.

263 For this purpose, let $\hat{\Omega}_f \subset \mathbb{R}^3$ be a fixed reference domain. We define a family of mappings:

$$264 \quad (2.5) \quad A_t^f : \hat{\Omega}_f \longrightarrow \Omega_f(t), \quad A_t^f : \mathbf{x}_0 \mapsto \mathbf{x},$$

265 where \mathbf{x} and \mathbf{x}_0 are the coordinates in the physical domain $\Omega_f(t)$ and the reference domain $\hat{\Omega}_f$,
 266 respectively. The fluid domain velocity \mathbf{w}_f is given by

$$267 \quad (2.6) \quad \mathbf{w}_f(t, \cdot) = \frac{dA_t^f}{dt}(t, A_t^f(t, \cdot)^{-1}).$$

269 Using this notation, we calculate the ALE time derivative of the fluid velocity:

$$270 \quad (2.7) \quad \partial_t \mathbf{u}_f|_{\mathbf{x}_0} = \partial_t \mathbf{u}_f(t, \mathbf{x}) + \mathbf{w}_f(t, \mathbf{x}) \cdot \nabla \mathbf{u}_f(t, \mathbf{x}), \text{ for } \mathbf{x} = A_t^f(\mathbf{x}_0), \mathbf{x}_0 \in \hat{\Omega}_f,$$

271 where $\partial_t \mathbf{u}_f|_{\mathbf{x}_0}$ denotes the time derivative in the reference configuration $\hat{\Omega}_f$. The incompressible
 272 Navier-Stokes equations in ALE form are given by the following:

$$273 \quad (2.8) \quad \left. \begin{aligned} & \rho_f \left(\frac{\partial \mathbf{u}_f}{\partial t} \Big|_{\hat{\mathbf{x}}_0} + (\mathbf{u}_f - \mathbf{w}_f) \cdot \nabla \mathbf{u}_f \right) = \nabla \cdot \boldsymbol{\sigma}_f(\mathbf{u}_f, p_f), \\ & \nabla \cdot \mathbf{u}_f = 0, \end{aligned} \right\} \text{in } \Omega_f(t) \times (0, T),$$

274 The ALE mapping defined in terms of the fluid domain displacement $\mathbf{d}(\mathbf{x}_0, t)$ is given by

$$A_t^f(\mathbf{x}_0) = \mathbf{x}_0 + \mathbf{d}(\mathbf{x}_0, t),$$

275 where we calculate $\mathbf{d}(\mathbf{x}_0, t)$ as the harmonic extension of the boundary data:

$$276 \quad \Delta \mathbf{d} = \mathbf{0} \quad \text{in } \hat{\Omega}_f, \quad \mathbf{d} = \boldsymbol{\eta} \quad \text{on } \hat{\Gamma}, \quad \mathbf{d} = \mathbf{0} \quad \text{on } \partial \hat{\Omega}_f / \hat{\Gamma}.$$

278 Here $\hat{\Omega}_f$ denotes the reference fluid domain, and $\hat{\Gamma}$ is the reference fluid-structure interface.

The coupling conditions for the fluid poroelastic structure interaction problem.

At the fluid-structure interface $\Gamma(t)$, we impose two kinematic coupling conditions, denoted by (K1) and (K2) below, and two dynamic coupling conditions, denoted by (D1) and (D2) below (see [12, 13]). The coupling conditions will be stated on the reference fluid-structure interface $\hat{\Gamma} = \partial \hat{\Omega}_f \cap \partial \hat{\Omega}_p$. The values of the fluid velocity \mathbf{u}_f below are assumed at the current interface $\Gamma(t)$, but evaluated on the reference configuration $\hat{\Gamma}$. The notation $\mathbf{u}_f|_{\Gamma(t)}$ on $\hat{\Gamma}$ used below means

$$\mathbf{u}_f|_{\Gamma(t)} = \mathbf{u}_f \circ A_t^f(\hat{\mathbf{x}}, t), \quad (\hat{\mathbf{x}}, t) \in \hat{\Gamma}.$$

279 The same holds for the normal stress $\boldsymbol{\sigma}_f \mathbf{n}$ on $\hat{\Gamma}$.

280 The coupling conditions are:

281 (K1) Continuity of normal components of fluid velocities describing fluid penetration into
 282 the poroelastic structure in the normal direction:

$$283 \quad (2.9) \quad \mathbf{u}_p \cdot \mathbf{n} = (\mathbf{u}_f|_{\Gamma(t)} - \frac{\partial \boldsymbol{\eta}}{\partial t}) \cdot \mathbf{n}, \quad \text{on } \hat{\Gamma} \times (0, T),$$

284 (K2) The Beavers-Joseph-Saffman condition describing slip between the fluid and structure
 285 velocities in the tangential direction, with parameter β denoting the slip length (the inverse of
 286 which describes friction) [26, 25], and J the Jacobian of the transformation between the Eulerian
 287 and Lagrangian frameworks:

$$288 \quad (2.10) \quad \beta \left(\mathbf{u}_f|_{\Gamma(t)} - \frac{\partial \boldsymbol{\eta}}{\partial t} \right) \cdot \mathbf{t}_i = -\mathbf{t}_i \cdot J \boldsymbol{\sigma}_f \mathbf{n}, \quad \text{on } \hat{\Gamma} \times (0, T), \quad i = 1, 2.$$

289 (D1) Continuity of dynamic pressure across the interface:

$$290 \quad (2.11) \quad \mathbf{n} \cdot J \boldsymbol{\sigma}_f \mathbf{n} + \rho_f \frac{|\mathbf{u}_f|_{\Gamma(t)}|^2}{2} = -p_p, \quad \text{on } \hat{\Gamma} \times (0, T),$$

291 (D2) The balance of contact forces:

$$292 \quad (2.12) \quad J \boldsymbol{\sigma}_f \mathbf{n} - \boldsymbol{\sigma}_p \mathbf{n} = 0, \quad \text{on } \hat{\Gamma} \times (0, T).$$

293 **The boundary and initial data.** The coupled FSI problem for blood plasma consists of
 294 the Navier-Stokes-Biot problem (2.1)-(2.2), with the coupling conditions (2.9)-(2.12), and the
 295 following boundary and initial data:

$$\begin{aligned}
(2.13) \quad & \mathbf{u}_f \cdot \mathbf{t} = 0, \quad P_{\text{in/out}}(t) = p_f + \frac{\rho_f}{2} |\mathbf{u}_f|^2 \text{ on } \Gamma_{\text{in/out}}^f \times (0, T) \\
& \boldsymbol{\eta} = \mathbf{0} \quad \text{on } \Gamma_{\text{in/out}}^f \cup \Gamma_{\text{ext}}^p \times (0, T), \quad \nabla p_p \cdot \mathbf{n}_p = 0 \text{ on } \Gamma_{\text{ext}}^p \times (0, T)
\end{aligned}$$

$$(2.14) \quad \mathbf{u}_f|_{t=0} = \mathbf{u}_f^0 \text{ in } \hat{\Omega}_f(0), \quad \boldsymbol{\eta}|_{t=0} = \partial_t \boldsymbol{\eta}|_{t=0} = \mathbf{0} \text{ in } \hat{\Omega}^p, \quad p_p|_{t=0} = 0 \text{ in } \hat{\Omega}^p.$$

No-slip boundary condition for the fluid is assumed on the (remaining) rigid part of the fluid

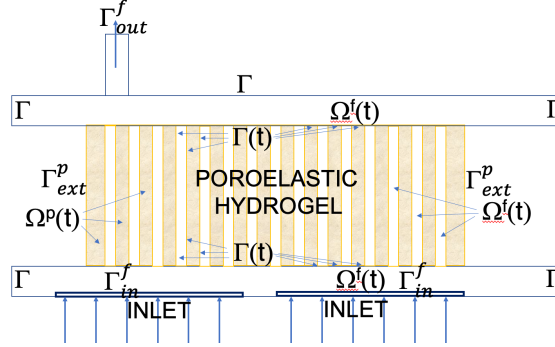


FIG. 7. A sketch of a 2D slice of the fluid and poroelastic structure domains together with their boundaries.

domain boundary, denoted by Γ in Fig. 7. In Fig. 7 we show the entire fluid and poroelastic structure domains (a 2D slice) together with their boundaries.

Inlet flow. To account for the presence of four nanopore-size permeable membranes at the inlet, we use an experimentally derived relationship between flow and pressure gradient (Darcy law) through nanoporous membranes, derived in [22]. More precisely, it was demonstrated in Shuvo Roy's lab, see [22], that silicon nanopore membranes with pore sizes of 7 nm generated a hydraulic permeability of 130 ml/hr/m²/mmHg. More generally, the results in [22] postulate the following experimentally validated nano-macro scale Darcy relationship between the nano pore membrane parameters and the macro-scale filtration flow parameters:

$$(2.15) \quad w = (12\mu h Q / n l \Delta p)^{\frac{1}{3}},$$

where w is the pore width, l is the pore length, h is the membrane thickness, n is the number of pores per (unit) membrane, μ is the viscosity, Q is the volumetric flow rate, and Δp is transmembrane pressure. This information was used to find the **macro-scale inlet flow based on the micro-scale parameters that are specific to membrane structure**. Namely, given the inlet pressure $P_{\text{in}}(t)$, the filtration flow through the membranes at time t^{n+1} was calculated via

$$(2.16) \quad \mathbf{u}^{n+1} \cdot \mathbf{n} = \frac{w^2}{12\mu h} (P_{\text{in}} - p_{\text{gasket}}^n) \text{ on } \Gamma_{\text{in}}^f,$$

where p_{gasket}^n is the gasket pressure at time t^n . Here we used that the total pore area for each membrane is given by $n l w$.

In addition to the micro-macro scale relationship (2.15) the work published in [22] demonstrated the feasibility of silicon nanopore membranes for immunoisolation, by measuring the selectivity against transport of cytokines and small molecules using the pressure-driven ultrafiltration system.

TABLE 1
Parameters for FSI simulations.

Parameter	Value
Blood inlet pressure (Average)(<i>mmHg</i>)	46
Blood outlet pressure (Average)(<i>mmHg</i>)	20
Channel height (<i>cm</i>)	0.3
Channel length (<i>cm</i>)	6.5
Channel width (<i>cm</i>)	0.7
Fluid density (<i>g / cm³</i>)	1
Fluid viscosity (<i>cm²/s</i>)	0.04
Poroelastic structure density (<i>g / cm³</i>)	1.2
Pressure storage coefficient c_0	1×10^{-7}
Permeability	2×10^{-4}
Young's modulus E (<i>d y n e s / cm²</i>)	$4 \times 10^4 \sim 0.75 \times 10^6$
Poisson's ratio σ	0.49
Biot-Willis parameter α	1×10^{-2}

323 Table 1 shows the parameter values used in this FSI model.

324 **Energy estimate.** To show that the coupled problem is well-defined in terms of having
 325 a bounded energy, which is related to stability, we show below that the total energy of the
 326 problem, and the total dissipation, are bounded by a constant that only depends on the initial
 327 and boundary data. In the energy estimate below we assume that $\boldsymbol{\kappa} = \kappa \mathbf{I}$, where κ may be a
 328 nonlinear bounded function of the fluid content $\zeta = \Phi - \Phi_0$ as in (2.4), or a bounded function of
 329 (x, y, z, t) . More precisely, using the approaches similar to the proof of Theorem 3.1 in [42] one
 330 can show that the following energy estimate holds.

331 **THEOREM 2.1.** *The energy of the coupled Navier-Stokes-Biot problem (2.1)-(2.2), (2.9)-(2.14),*
 332 *satisfies the following inequality:*

333 (2.17)
$$\frac{d}{dt} E(t) + D(t) \leq C(t),$$

334 where $E(t)$ denotes the kinetic energy of fluid and the kinetic and elastic energy of the poroelastic
 335 structure:

336
$$E(t) = \frac{\rho_f}{2} \|\mathbf{u}_f\|_{L^2(\Omega_f(t))}^2 + \frac{\rho_p}{2} \|\partial_t \boldsymbol{\eta}\|_{L^2(\hat{\Omega}_p)}^2 + \frac{c_0}{2} \|p_p\|_{L^2(\hat{\Omega}_p)}^2 + \mu_p \|\mathbf{D}(\boldsymbol{\eta})\|_{L^2(\hat{\Omega}_p)}^2 + \frac{\lambda_p}{2} \|\nabla \cdot \boldsymbol{\eta}\|_{L^2(\hat{\Omega}_p)}^2$$

338 and $D(t)$ denotes the total dissipation:

339
$$D(t) = \mu_f \|\mathbf{D}(\mathbf{u}_f)\|_{L^2(\Omega_f(t))}^2 + \|\kappa^{\frac{1}{2}} \nabla p_p\|_{L^2(\hat{\Omega}_p)}^2 + \beta \|(\mathbf{u}_f - \partial_t \boldsymbol{\eta}) \cdot \mathbf{t}\|_{L^2(\hat{\Gamma})}^2,$$

341 and $C(t)$ depends only on the initial and boundary data.

342 **2.2. Coupled models for oxygen concentration.** We present two models for oxygen
 343 concentration, both defined on moving domains obtained from the fluid-structure interaction
 344 problem discussed above. One is an advection-diffusion equation for the concentration $C_f(\mathbf{x}, t)$
 345 of oxygen in the fluid channel/gasket, defined on $\Omega_f(t)$, and the other is a nonlinear advection-
 346 reaction-diffusion equation for oxygen concentration in the scaffold, $C_p(\mathbf{x}, t)$, defined on $\Omega_p(t)$.
 347 The two models are coupled at the interface $\Gamma(t)$ separating the gasket flow from the poroelastic
 348 scaffold. The oxygen concentration models are coupled to the fluid-structure interaction problem
 349 above via the advection velocity obtained from the FSI problem above, and via the fluid domain

350 motion. This is a one-way coupling because nothing from the problem for oxygen concentration
 351 influences the solution of the FSI problem.

352 The advection-diffusion for the concentration C_f of **oxygen in the fluid channel/gasket**
 353 written in conservation form reads:

$$354 \quad (2.18) \quad \frac{\partial C_f}{\partial t} + \nabla \cdot (\mathbf{u}_f C_f) - \nabla \cdot (D_f \nabla C_f) = 0, \text{ in } \Omega_f(t) \times (0, T),$$

355 where the advection velocity \mathbf{u}_f is given by the solution of the Navier-Stokes equations in domain
 356 $\Omega_f(t)$. Here, D_f is the free oxygen diffusion coefficient ($D_f = 2.41 \times 10^{-5} \text{cm}^2 \text{s}^{-1}$) in blood [5].
 357 This model is coupled to the gasket fluid flow model via the fluid advection velocity \mathbf{u}_f obtained
 358 from the Navier-Stokes equations (2.1), and via the fluid domain motion $\Omega_f(t)$.

359 The nonlinear advection-reaction-diffusion equation for concentration C_p of **oxygen in the**
 360 **hydrogel** is defined on the *moving domain* $\Omega_p(t)$. Thus, the advection velocity in this case must
 361 be given by the *sum* of the *relative* filtration velocity \mathbf{u}_p , obtained from the Biot equations (2.2),
 362 *plus* the velocity of the motion of the hydrogel skeleton:

$$363 \quad (2.19) \quad \mathbf{w}_p = \partial_t \boldsymbol{\eta}.$$

364 Therefore, we introduce

$$365 \quad (2.20) \quad \tilde{\mathbf{u}}_p = \mathbf{u}_p + \mathbf{w}_p$$

366 and write the equation for oxygen concentration C_p in the poroelastic hydrogel on the moving
 367 domain $\Omega_p(t)$ in conservation form as follows:

$$368 \quad (2.21) \quad \frac{\partial C_p}{\partial t} + \nabla \cdot (\tilde{\mathbf{u}}_p C_p) = \nabla \cdot (D_p \nabla C_p) + R_{\max} \frac{C_p}{C_p + C_{MM}} \mathcal{H}(C_p > C_{cr}), \text{ in } \hat{\Omega}_p(t) \times (0, T),$$

369 where R_{\max} is the maximum oxygen consumption rate, C_{MM} is the Michaelis-Menten constant
 370 corresponding to the oxygen concentration where consumption drops to 50% of its maximum
 371 [7], C_{cr} is the critical oxygen concentration below which necrosis is assumed to occur after a
 372 sufficiently long exposure, and \mathcal{H} is the Heaviside step-down function to account for the ceasing
 373 of consumption in those parts of the tissue where the oxygen concentration fell below a critical
 374 concentration C_{cr} [7, 8]. D_p is the diffusion coefficient of oxygen, whose value has been estimated
 375 for rat pancreatic islets to be $1.3 \times 10^{-9} \text{cm}^2 \text{s}^{-1}$.

376 **The ALE formulation of the oxygen concentration models.** Before we rewrite equa-
 377 tions (2.18) and (2.21) in ALE form, we recall that the advection in (2.21) is driven by the
 378 plasma filtration velocity $\tilde{\mathbf{u}}_p = \mathbf{u}_p + \mathbf{w}_p$, where \mathbf{u}_p is the relative filtration velocity obtained from
 379 the Biot model defined on $\hat{\Omega}_p$. Namely, \mathbf{u}_p denotes the composite function between the relative
 380 filtration velocity defined on $\hat{\Omega}_p$ and the inverse of the ALE mapping $\mathcal{A}_t^p : \hat{\Omega}_p \rightarrow \Omega_p(t)$ associated
 381 with the motion of the poroelastic matrix $\mathcal{A}_t^p : \mathbf{x}_0 \mapsto \mathbf{x}_0 + \boldsymbol{\eta}(\mathbf{x}_0, t)$. Therefore, $\tilde{\mathbf{u}}_p = \mathbf{u}_p + \mathbf{w}_p$,
 382 where $\mathbf{u}_p = \mathcal{A}_t^p \circ \mathbf{u}_p|_{\hat{\Omega}} \left((\mathcal{A}_t^p)^{-1} \mathbf{x}, t \right)$ and $\mathbf{w}_p = \partial_t \boldsymbol{\eta}$.

383 Equation (2.18), defined on the current moving domain $\Omega_f(t) \times (0, T)$ in ALE form reads:

$$384 \quad (2.22) \quad \frac{\partial C_f}{\partial t} \Big|_{\mathbf{x}_0} - \nabla \cdot (D_f \nabla C_f) + (\mathbf{u}_f - \mathbf{w}_f) \cdot \nabla C_f = 0,$$

385 where \mathbf{w}_f is the fluid domain velocity.

386 Equation (2.21), defined on the current moving domain $\Omega_p(t) \times (0, T)$, in ALE form reads:

$$387 \quad (2.23) \quad \frac{\partial C_p}{\partial t} \Big|_{\mathbf{x}_0} - \mathbf{w}_p \cdot \nabla C_p + \nabla \cdot (\tilde{\mathbf{u}}_p C_p) - \nabla \cdot (D_p \nabla C_p) = R_{\max} \frac{C_p}{C_p + C_{MM}} \delta(C_p > C_{cr}).$$

388 Notice that the time derivatives of oxygen concentration $\frac{\partial C_f}{\partial t}|_{\mathbf{x}_0}$ and $\frac{\partial C_p}{\partial t}|_{\mathbf{x}_0}$ are evaluated on the
 389 corresponding reference domains and then mapped back onto the corresponding moving domains
 390 where the ALE equations are defined.

391 In conservation form, equations (2.22) and (2.23) above read as follows.

392 **On $\Omega_f(t) \times (0, T)$ we have:**

$$393 \quad (2.24) \quad \frac{\partial C_f}{\partial t}|_{\mathbf{x}_0} + \nabla \cdot [(\mathbf{u}_f - \mathbf{w}_f) C_f - D_f \nabla C_f] + (\nabla \cdot \mathbf{w}_f) C_f = 0,$$

394 where ALE velocity \mathbf{w}_f is given by (2.6).

395 **On $\Omega_p(t) \times (0, T)$ we have:**

$$396 \quad (2.25) \quad \frac{\partial C_p}{\partial t}|_{\mathbf{x}_0} + \nabla \cdot [(\tilde{\mathbf{u}}_p - \mathbf{w}_p) C_p - D_p \nabla C_p] + (\nabla \cdot \mathbf{w}_p) C_p = R_{\max} \frac{C_p}{C_p + C_{MM}} \mathcal{H}(C_p > C_{cr}),$$

397 where \mathbf{w}_p is given by (2.19).

Coupling conditions. Two equations (2.22) and (2.23) are coupled across the moving inter-
 face $\Gamma(t)$ via the following two coupling conditions, describing continuity of oxygen concentration
 across the interface and continuity of total oxygen fluxes:

$$\left. \begin{aligned} C_f &= C_p \\ [(\mathbf{u}_f - \mathbf{w}_f) C_f - D_f \nabla C_f] \cdot \mathbf{n}_f &= [(\tilde{\mathbf{u}}_p - \mathbf{w}_p) C_p - D_p \nabla C_p] \cdot \mathbf{n}_f \end{aligned} \right\} \text{ on } \Gamma(t) \times (0, T).$$

398 Because of the kinematic coupling condition at the interface $\mathbf{u}_p \cdot \mathbf{n} = \left(\mathbf{u}_f|_{\Gamma(t)} - \frac{\partial \boldsymbol{\eta}}{\partial t} \right) \cdot \mathbf{n}$ and
 399 the fact that $\mathbf{w}_f = \partial_t \boldsymbol{\eta}$ at the interface and that $\tilde{\mathbf{u}}_p - \mathbf{w}_p = \mathbf{u}_p$ is the relative filtration velocity
 400 with respect to the motion of the poroelastic matrix, after using the continuity of concentrations
 401 $C_f = C_p$ at the interface, one obtains the following coupling conditions:

$$402 \quad (2.26) \quad \left. \begin{aligned} C_f &= C_p \\ D_f \nabla C_f \cdot \mathbf{n}_f &= D_p \nabla C_p \cdot \mathbf{n}_f \end{aligned} \right\} \text{ on } \Gamma(t) \times (0, T).$$

403 **Initial and boundary conditions.** The coupled system (2.22), (2.23) and (2.26) is sup-
 404 plemented with the following initial and boundary conditions:

$$405 \quad (2.27) \quad C_f = C_{f,0}, \text{ in } \Omega_f \times \{t = 0\}, \quad C_p = C_{p,0}, \text{ in } \Omega_p \times \{t = 0\}$$

$$407 \quad (2.28) \quad C_f = C_{inlet}, \text{ on } \Gamma_{in}^f, \quad D_f \nabla C_f \cdot \mathbf{n}_f = 0, \text{ on } \Gamma_{out}^f, \quad D_p \nabla C_p \cdot \mathbf{n}_p = 0, \text{ on } \Gamma_{ext}^p,$$

408 where $C_{f,0}$ and $C_{p,0}$ are initial concentrations in the fluid channel and hydrogel respectively,
 409 which are assumed to be zero. Here, Γ_{in}^f and Γ_{out}^f denote the fluid channel inlet and outlet, and
 410 Γ_{ext}^p denotes external sidewalls of the hydrogel, where we assume that oxygen cannot penetrate
 411 the external sidewalls. All the parameters used in the simulations are obtained from [7, 8] and
 412 reported in Table 2.

413 **Energy Estimate.** The following energy estimate shows that the coupled advection-
 414 reaction-diffusion problem for oxygen concentration (2.24)-(2.28) is well-defined in terms of hav-
 415 ing a bounded energy.

416 **THEOREM 2.2.** *Let $\tilde{\mathbf{u}}_p \in L^2(0, T; L^2(\Omega_p(t)))$ and $\nabla \cdot \tilde{\mathbf{u}}_p \in L^2(0, T; L^2(\Omega_p(t)))$. Then, there*
 417 *exist $K(t) > 0$, $\tilde{C}(t) > 0$, and $\tilde{D}_p > 0$ such that the coupled advection-reaction-diffusion problem*
 418 *(2.24)-(2.28) satisfies the following energy estimate:*

$$419 \quad (2.29) \quad \|C_f\|_{L^2(\Omega_f(t))}^2 + \|C_p\|_{L^2(\Omega_p(t))}^2 + 2 \int_0^t \|D_f \nabla C_f\|_{L^2(\Omega_f(\tau))}^2 d\tau + 2 \int_0^t \|\tilde{D}_p \nabla C_p\|_{L^2(\Omega_p(\tau))}^2 d\tau$$

$$420 \quad (2.30) \quad \leq K(t) e^{2 \int_0^t \tilde{C}(\tau) d\tau},$$

422 where $\tilde{C}(t)$ depends on $\|\nabla \cdot \tilde{\mathbf{u}}_p\|_{L^2(\Omega_p(t))}^2$, and $K(t)$ depends on the initial data and on $\tilde{C}(t)$.

423 The proof of this energy estimate is similar to the proof of Theorem 3.2 in [42].

TABLE 2
Parameters for the coupled convection-reaction-diffusion problem.

Parameters	Value (units)
Concentration of oxygen at fluid inlet C_{inlet}	$2 \times 10^{-7} \text{ (mol} \cdot \text{cm}^{-3})$ [17]
Diffusion coefficient in fluid channel D_f	$3.0 \times 10^{-5} \text{ (cm}^2 \cdot \text{s}^{-1})$
Diffusion coefficient in hydrogel D_p	$1.3 \times 10^{-5} \text{ (cm}^2 \cdot \text{s}^{-1})$
Maximum oxygen consumption rate R_{max}	$3.4 \times 10^{-8} \text{ (mol} \cdot \text{cm}^{-3} \cdot \text{s}^{-1})$
Critical oxygen concentration C_{cr}	$1.0 \times 10^{-10} \text{ (mol} \cdot \text{cm}^{-3})$
The Michaelis-Menten constant C_{MM}	$1.0 \times 10^{-9} \text{ (mol} \cdot \text{cm}^{-3})$

424 **3. Discretized problems and numerical schemes.** We use Finite Element Method-
 425 based schemes to solve the FSI problem (2.1)-(2.13) and the coupled advection-reaction-diffusion
 426 problem for oxygen concentration (2.22), (2.23) and (2.26) on moving domains. For the FSI
 427 problem we introduce a new scheme based on Nitsche’s method, which improves the already
 428 existing schemes in the following two ways: the proposed method has accuracy *higher than 1st*
 429 *order* and it solves a *nonlinearly coupled* problem between the Navier-Stokes equations defined
 430 on *moving domain* and the Biot equations. We also prove that this new numerical scheme is
 431 *unconditionally stable*.

432 To couple the macro-scale simulations with the micro-scale information, we use Smoothed
 433 Particle Hydrodynamics (SPH) simulations. In particular, we recover the information about
 434 hydraulic permeability locally, for every small “control” volume, for a given hydrogel structure,
 435 and use it to recover the global, macro-scale permeability tensor κ . To avoid time-consuming and
 436 computationally expensive SPH simulations for every new hydrogel structure, we use Convolution
 437 Neural Networks, trained on a set of our synthetic data (calculated off line), to obtain κ for new
 438 hydrogel structures which are either generated synthetically (using our numerical simulations
 439 with random pore distributions), or for the actual hydrogel structures that can be imaged using
 440 high precision laser scanning confocal microscopy.

441 Details are presented next.

442 **3.1. Discretization of the fluid-structure interaction problem.** We discretize and
 443 solve the FSI problem involving poroelastic structure in a monolithic way, using the refactorized
 444 Cauchy’s ‘ θ -like’ method for the time discretization (see [14]), which is equivalent to the midpoint
 445 method when $\theta = \frac{1}{2}$. In this case the method is conservative and second-order accurate in
 446 time. To discretize the problem in space, we use $\mathbb{P}_2 - \mathbb{P}_1$ elements for the fluid velocity and
 447 pressure, and \mathbb{P}_2 elements for the structure displacement and velocity, and $\mathbb{P}_2 - \mathbb{P}_1$ for the Biot
 448 filtration velocity and pressure. Note, again, that the fluid-structure interaction problem and the
 449 advection-reaction-diffusion problem are defined on moving domains.

450 To enforce the coupling conditions, we use Nitsche’s method, similar to [12]. In [12] the
 451 Nitsche’s method was first-order accurate in time, and it was applied to solve a Stokes-Biot
 452 coupled problem where the coupling was assumed across a *fixed* interface, i.e., linear coupling.
 453 In [42] this method was extended to a Navier-Stokes-Biot coupled problem with the coupling
 454 assumed across the *current, moving interface*, i.e., nonlinear coupling, with first-order accuracy
 455 in time. In the present work, we extend this method to improve the time-accuracy to second-
 456 order, and we prove that the proposed method is *unconditionally stable*. Before we present the
 457 discretized problem, we first state the continuous weak formulation.

458 **Weak formulation.** We solve the coupled FSI problem (2.1)-(2.2), with the coupling condi-
 459 tions (2.9)-(2.12), and the initial and boundary conditions (2.14) and (2.13) in mixed formulation
 460 (see e.g., [12, 3, 30] for the Stokes-Biot mixed formulation). The corresponding continuous **weak**

461 **formulation** is given by the following:

$$\begin{aligned}
 & -\rho_f \int_0^T \int_{\Omega_f(t)} \mathbf{u}_f \cdot \partial_t \phi_f d\mathbf{x}dt + \rho_f \int_0^T \int_{\Omega_f(t)} (\mathbf{u}_f \cdot \nabla) \mathbf{u}_f \cdot \phi_f d\mathbf{x}dt - \rho_p \int_0^T \int_{\hat{\Omega}_p} \dot{\boldsymbol{\eta}} \cdot \partial_t \boldsymbol{\xi}_p d\mathbf{x}dt \\
 & + 2\mu_f \int_0^T \int_{\Omega_f(t)} \mathbf{D}(\mathbf{u}_f) : \mathbf{D}(\phi_f) d\mathbf{x}dt + \int_0^T \int_{\hat{\Omega}_p} 2\mu_s \mathbf{D}(\boldsymbol{\eta}) : \mathbf{D}(\boldsymbol{\xi}_p) + \lambda_p (\nabla \cdot \boldsymbol{\eta}) (\nabla \cdot \boldsymbol{\xi}_p) d\mathbf{x}dt \\
 & - \alpha \int_0^T \int_{\hat{\Omega}_p} p_p (\nabla \cdot \boldsymbol{\xi}_p) d\mathbf{x}dt - \rho_p \int_0^T \int_{\hat{\Omega}_p} \boldsymbol{\eta} \cdot \partial_t \boldsymbol{\varphi}_p d\mathbf{x}dt - \rho_p \int_0^T \int_{\hat{\Omega}_p} \dot{\boldsymbol{\eta}} \cdot \boldsymbol{\varphi}_p d\mathbf{x}dt \\
 462 & + c_0 \int_0^T \int_{\hat{\Omega}_p} p_p \partial_t \psi_p d\mathbf{x}dt + \int_0^T \int_{\hat{\Omega}_p} (\nabla \cdot \mathbf{u}_p) \psi_p d\mathbf{x}dt + \alpha \int_0^T \int_{\hat{\Omega}_p} (\nabla \cdot \partial_t \boldsymbol{\eta}) \psi_p d\mathbf{x}dt \\
 & + \int_0^T \int_{\hat{\Omega}_p} \frac{1}{\kappa} \mathbf{u}_p \cdot \boldsymbol{\phi}_p d\mathbf{x}dt - \int_0^T \int_{\hat{\Omega}_p} p_p (\nabla \cdot \boldsymbol{\phi}_p) d\mathbf{x}dt + \int_0^T I_{\hat{\Gamma}}^{\text{bdry}}(t) dt \\
 & = \int_0^T \int_{\Gamma_{in}^f} P_{in}(t) (\boldsymbol{\phi}_f \cdot \mathbf{n}) d\mathbf{S}dt - \int_0^T \int_{\Gamma_{out}^f} P_{out}(t) (\boldsymbol{\phi}_f \cdot \mathbf{n}) d\mathbf{S}dt + \int_0^T \int_{\hat{\Omega}_p} (\mathbf{F}^s \cdot \boldsymbol{\xi}_p + F_p \psi^p) d\mathbf{x}dt \\
 463 & + \int_{\Omega_f(t)} (\mathbf{u}_f \cdot \boldsymbol{\phi}_f)|_{t=0} d\mathbf{x} + \int_{\hat{\Omega}_p} (\dot{\boldsymbol{\eta}} \cdot \boldsymbol{\xi}_p)|_{t=0} d\mathbf{x} + \int_{\hat{\Omega}_p} (\boldsymbol{\eta} \cdot \boldsymbol{\varphi}_p)|_{t=0} d\mathbf{x} + \int_{\hat{\Omega}_p} (p_p \partial_t \psi_p)|_{t=0} d\mathbf{x}
 \end{aligned}$$

464 where

$$465 \quad I_{\hat{\Gamma}}^{\text{bdry}}(t) = \beta \sum_{i=1,2} \int_{\hat{\Gamma}} (\mathbf{t}_i \cdot (\mathbf{u}_f - \partial_t \boldsymbol{\eta})) (\mathbf{t}_i \cdot \boldsymbol{\phi}_f - \mathbf{t}_i \cdot \boldsymbol{\xi}_p) d\mathbf{S} + \int_{\hat{\Gamma}} \frac{\rho_f}{2} |\mathbf{u}_f|^2 (\boldsymbol{\phi}_p \cdot \mathbf{n}) d\mathbf{S}.$$

467 The vectors $\mathbf{t}_i, i = 1, 2$ are two linearly independent tangent vectors at the interface. The
 468 kinematic coupling condition (2.9) must be included in the solution and test function spaces, and
 469 is numerically enforced by Nitsche's penalization [12].

470 The function spaces for the fluid velocity are denoted by $V^f(t)$ and $V_{\text{div}}^f(t)$ below, and the
 471 function space for the pressure is denoted by $Q^f(t)$, all defined on $\Omega_f(t)$. The functions spaces
 472 for the filtration velocity and fluid pore pressure are denoted by V^p and Q^p below, both defined
 473 on $\hat{\Omega}_p$, and the function spaces for the structure displacement and velocity are denoted by X^p
 474 and \dot{X}^p , both defined on $\hat{\Omega}_p$. The spaces are defined as follows:

$$\begin{aligned}
 & V^f(t) = \{\mathbf{v} \in [H^1(\Omega_f(t))]^d \mid \mathbf{v} \cdot \mathbf{t} = 0 \text{ on } \Gamma_{in}^f \cup \Gamma_{out}^f, \mathbf{v} = \mathbf{0} \text{ on } \Gamma_{ext}^f\}, \\
 475 & (3.1) \quad V_{\text{div}}^f(t) = \{\mathbf{v} \in V^f(t) \mid \nabla \cdot \mathbf{v} = 0\}, \quad Q^f(t) = L^2(\Omega_f(t)), \\
 & V^p = \{\mathbf{u}_p \in H(\text{div}, \hat{\Omega}_p) \mid \mathbf{u}_p \cdot \mathbf{n}_p = 0\} = \{\mathbf{u}_p \in [L^2(\hat{\Omega}_p)]^d \mid \nabla \cdot \mathbf{u}_p \in L^2(\hat{\Omega}_p), \mathbf{u}_p \cdot \mathbf{n}_p = 0\}, \\
 476 & Q^p = L^2(\hat{\Omega}_p), \quad X^p = [H^1(\hat{\Omega}_p)]^d, \quad \dot{X}^p = [L^2(\hat{\Omega}_p)]^d.
 \end{aligned}$$

477 We further introduce the following Bochner spaces:

$$\begin{aligned}
 478 & W^f = L^\infty(0, T; L^2(\Omega_f(t))) \cap L^2(0, T; V_{\text{div}}^f(t)), \quad \mathcal{X}^p = L^\infty(0, T; X^p), \\
 480 & \dot{\mathcal{X}}^p = L^\infty(0, T; \dot{X}^p), \quad \mathcal{Q}^p = L^\infty(0, T; L^2(\hat{\Omega}_p)) \cap L^2(0, T; Q^p), \quad \mathcal{V}^p = L^2(0, T; V^p).
 \end{aligned}$$

The function space for the solution of the FSI problem is then defined by:

$$\mathcal{S} = \{(\mathbf{u}_f, \mathbf{u}_p, p_p, \boldsymbol{\eta}, \dot{\boldsymbol{\eta}}) \in (W^f \times \mathcal{V}^p \times \mathcal{Q}^p \times \mathcal{X}^p \times \dot{\mathcal{X}}^p) \mid \mathbf{u}_p \cdot \mathbf{n} = (\mathbf{u}_f|_{\Gamma(t)} - \partial_t \boldsymbol{\eta}) \cdot \mathbf{n} \text{ on } \hat{\Gamma}\},$$

481 with the corresponding test space:

$$\begin{aligned}
 482 & \mathcal{T} = \{(\phi_f, \boldsymbol{\phi}_p, \psi_p, \boldsymbol{\varphi}_p, \boldsymbol{\xi}_p) \in C_c^1([0, T]; V_{\text{div}}^f(t) \times V^p \times Q^p \times X^p \times \dot{X}^p) \\
 483 & \quad \mid \boldsymbol{\phi}_p \cdot \mathbf{n} = (\phi_f|_{\Gamma(t)} - \partial_t \boldsymbol{\varphi}_p) \cdot \mathbf{n} \text{ on } \hat{\Gamma}\}.
 \end{aligned}$$

485 In this case, instead of the homogeneous Dirichlet boundary condition for Darcy pressure on
 486 Γ_{ext} , we impose the condition on Darcy velocity $\mathbf{u}_p \cdot \mathbf{n} = 0$ on Γ_{ext} . We present the discretized
 487 problem based on this weak formulation next.

488 **Discretization.** Let the shape of $\Omega_f(t)$ and $\hat{\Omega}_p$ be polygons/tetrahedra. Denote by h the
 489 characteristic mesh size and suppose that T_h^f and T_h^p are the uniform conforming triangulation
 490 of $\Omega_f(t)$ and $\hat{\Omega}_p$, respectively. Based on the meshes, we define the finite element spaces $V_h^f \subset$
 491 $V^f, Q_h^f \subset Q^f, V_h^p \subset V^p, Q_h^p \subset Q^p, X_h^p \subset X^p, \dot{X}_h^p \subset \dot{X}^p$ for the spatial discretization, where the
 492 function spaces V^f, V^p, Q^p, X^p , and \dot{X}^p are defined in (3.1).

493 Below, we will use Nitsche's method to enforce the coupling conditions at the discrete level.
 494 In particular, in Step 1 below, we introduce a *penalty parameter* $\gamma_f > 0$ to enforce the kinematic
 495 coupling condition. In Step 1 below we also introduce a flag $\varsigma \in \{1, 0, -1\}$ which determines
 496 whether a symmetric, incomplete, or skew-symmetric formulation is adopted [12] in the formu-
 497 lation.

498 More precisely, let $t^n = n\Delta t$ for $n = 0, \dots, N$, where Δt denotes the time step, and $t^{n+\theta} =$
 499 $t^n + \theta\Delta t$, for any $\theta \in [\frac{1}{2}, 1]$, and for all $n \geq 0$. The fully discretized coupled FSI problem in ALE
 500 form and the numerical scheme to solve it, are given by the following three steps.

501
 502

503 **STEP 1:** Given $\mathbf{u}_{f,h}^n, \mathbf{w}^n, \dot{\boldsymbol{\eta}}_h^n, \boldsymbol{\eta}_h^n, p_{p,h}^n$, compute $\mathbf{u}_{f,h}^{n+\theta}, p_{f,h}^{n+\theta}, \dot{\boldsymbol{\eta}}_h^{n+\theta}, \mathbf{u}_{p,h}^{n+\theta}, p_{p,h}^{n+\theta}$, such that

$$\begin{aligned}
 504 \quad (3.2) \quad & \rho_f \int_{\Omega_f^n} \frac{\mathbf{u}_{f,h}^{n+\theta} - \mathbf{u}_{f,h}^n}{\theta\Delta t} \cdot \boldsymbol{\phi}_{f,h} d\mathbf{x} + \rho_f \int_{\Omega_f^n} ((\mathbf{u}_{f,h}^n - \mathbf{w}^n) \cdot \nabla) \mathbf{u}_{f,h}^{n+\theta} \cdot \boldsymbol{\phi}_{f,h} d\mathbf{x} \\
 505 & + \int_{\Omega_f^n} \psi_{f,h} \nabla \cdot \mathbf{u}_{f,h}^{n+\theta} d\mathbf{x} - \int_{\Omega_f^n} p_{f,h}^{n+\theta} \nabla \cdot \boldsymbol{\phi}_{f,h} d\mathbf{x} + 2\mu_f \int_{\Omega_f^n} \mathbf{D}(\mathbf{u}_{f,h}^{n+\theta}) : \mathbf{D}(\boldsymbol{\phi}_{f,h}) d\mathbf{x} \\
 506 & + \rho_p \int_{\hat{\Omega}_p} \frac{\dot{\boldsymbol{\eta}}_h^{n+\theta} - \dot{\boldsymbol{\eta}}_h^n}{\theta\Delta t} \cdot \boldsymbol{\xi}_{p,h} d\mathbf{x} + 2\mu_s \int_{\hat{\Omega}_p} \mathbf{D}(\theta\Delta t \dot{\boldsymbol{\eta}}_h^{n+\theta} + \boldsymbol{\eta}_h^n) : \mathbf{D}(\boldsymbol{\xi}_{p,h}) d\mathbf{x} \\
 507 & + \lambda_p \int_{\hat{\Omega}_p} (\nabla \cdot (\theta\Delta t \dot{\boldsymbol{\eta}}_h^{n+\theta} + \boldsymbol{\eta}_h^n)) (\nabla \cdot \boldsymbol{\xi}_{p,h}) d\mathbf{x} - \alpha \int_{\hat{\Omega}_p} p_{p,h}^{n+\theta} (\nabla \cdot \boldsymbol{\xi}_{p,h}) d\mathbf{x} \\
 508 & + c_0 \int_{\hat{\Omega}_p} \frac{p_{p,h}^{n+\theta} - p_{p,h}^n}{\theta\Delta t} \psi_{p,h} d\mathbf{x} + \alpha \int_{\hat{\Omega}_p} (\nabla \cdot \dot{\boldsymbol{\eta}}_h^{n+\theta}) \psi_{p,h} d\mathbf{x} + \int_{\hat{\Omega}_p} (\nabla \cdot \mathbf{u}_{p,h}^{n+\theta}) \psi_{p,h} d\mathbf{x} \\
 509 & + \int_{\hat{\Omega}_p} (\boldsymbol{\kappa}^n)^{-1} \mathbf{u}_{p,h}^{n+\theta} \cdot \boldsymbol{\phi}_{p,h} d\mathbf{x} - \int_{\hat{\Omega}_p} p_{p,h}^{n+\theta} (\nabla \cdot \boldsymbol{\phi}_{p,h}) d\mathbf{x} - I_h^{*,n+\theta} \\
 510 & = \int_{\Gamma_{in}^f} P_{in}^{n+\theta} (\boldsymbol{\phi}_{f,h} \cdot \mathbf{n}) d\mathcal{S} - \int_{\Gamma_{out}^f} P_{out}^{n+\theta} (\boldsymbol{\phi}_{f,h} \cdot \mathbf{n}) d\mathcal{S}, \\
 511 &
 \end{aligned}$$

512 where

$$513 \quad I_h^{*,n+\theta} = [I_{\Gamma}^{\text{bdry}}]^{n+\theta} + [I_{\Gamma}^{\text{Nitsche}}]^{n+\theta},$$

514 with

$$\begin{aligned}
 [I_{\hat{\Gamma}}^{\text{bdry}}]^{n+\theta} &:= \int_{\hat{\Gamma}} (\mathbf{n} \cdot \boldsymbol{\sigma}_f \mathbf{n}_h^{n+\theta}) (\boldsymbol{\phi}_{f,h} \cdot \mathbf{n} - \boldsymbol{\xi}_{p,h} \cdot \mathbf{n} - \boldsymbol{\phi}_{p,h} \cdot \mathbf{n}) d\mathbf{S} \\
 &\quad - \beta \int_{\hat{\Gamma}} (\mathbf{u}_{f,h}^{n+\theta} - \dot{\boldsymbol{\eta}}_h^{n+\theta}) \cdot \mathbf{t} (\boldsymbol{\phi}_{f,h} - \boldsymbol{\xi}_{p,h}) \cdot \mathbf{t} d\mathbf{S} \\
 (3.3) \quad &\quad + \frac{\rho_f}{2} \int_{\hat{\Gamma}} |\mathbf{u}_f^n|^2 (\boldsymbol{\phi}_{p,h} \cdot \mathbf{n}^{n+\theta}) d\mathbf{S} \\
 [I_{\hat{\Gamma}}^{\text{Nitsche}}]^{n+\theta} &:= - \int_{\hat{\Gamma}} \gamma_f \mu_f h^{-1} \left[(\mathbf{u}_{f,h}^{n+\theta} - \mathbf{u}_{p,h}^{n+\theta} - \dot{\boldsymbol{\eta}}_h^{n+\theta}) \cdot \mathbf{n} (\boldsymbol{\phi}_{f,h} - \boldsymbol{\xi}_{p,h} - \boldsymbol{\phi}_{p,h}) \cdot \mathbf{n} \right] d\mathbf{S} \\
 &\quad + \int_{\hat{\Gamma}} \mathbf{n} \cdot \mathbf{J} \boldsymbol{\sigma}_f (\zeta \boldsymbol{\phi}_f, -\psi_f) \mathbf{n} (\mathbf{u}_{f,h}^{n+\theta} - \mathbf{u}_{p,h}^{n+\theta} - \dot{\boldsymbol{\eta}}_h^{n+\theta}) \cdot \mathbf{n} d\mathbf{S}.
 \end{aligned}$$

516

 From $\dot{\boldsymbol{\eta}}_h^{n+\theta}$ we calculate $\boldsymbol{\eta}_h^{n+\theta}$ using:

$$\dot{\boldsymbol{\eta}}_h^{n+\theta} = \frac{\boldsymbol{\eta}_h^{n+\theta} - \boldsymbol{\eta}_h^n}{\theta \Delta t}.$$

 517 STEP 2: Compute $\mathbf{u}_{f,h}^{n+1}, \dot{\boldsymbol{\eta}}_h^{n+1}, \boldsymbol{\eta}_h^{n+1}, p_{p,h}^{n+1}$, as

$$\begin{aligned}
 518 \quad \mathbf{u}_{f,h}^{n+1} &= \frac{1}{\theta} \mathbf{u}_{f,h}^{n+\theta} - \frac{1-\theta}{\theta} \mathbf{u}_{f,h}^n && \text{in } \Omega_f^n, \\
 519 \quad \boldsymbol{\eta}_h^{n+1} &= \frac{1}{\theta} \boldsymbol{\eta}_h^{n+\theta} - \frac{1-\theta}{\theta} \boldsymbol{\eta}_h^n && \text{in } \hat{\Omega}_p, \\
 520 \quad \dot{\boldsymbol{\eta}}_h^{n+1} &= \frac{1}{\theta} \dot{\boldsymbol{\eta}}_h^{n+\theta} - \frac{1-\theta}{\theta} \dot{\boldsymbol{\eta}}_h^n && \text{in } \hat{\Omega}_p, \\
 521 \quad p_{p,h}^{n+1} &= \frac{1}{\theta} p_{p,h}^{n+\theta} - \frac{1-\theta}{\theta} p_{p,h}^n && \text{in } \hat{\Omega}_p. \\
 522
 \end{aligned}$$

 523 STEP 3: Update the fluid mesh by solving the following problem

$$\begin{aligned}
 524 \quad -\Delta \boldsymbol{\eta}_f^{n+1} &= 0 && \text{in } \hat{\Omega}_f \\
 525 \quad \boldsymbol{\eta}_f^{n+1} &= 0 && \text{on } \hat{\Gamma}_{in/out}^f, \\
 526 \quad \boldsymbol{\eta}_f^{n+1} &= \boldsymbol{\eta}^{n+1} && \text{on } \hat{\Gamma}, \\
 527 \quad \mathbf{w}^{n+1} &= \frac{\boldsymbol{\eta}_f^{n+1} - \boldsymbol{\eta}_f^n}{\theta \Delta t} && \text{in } \hat{\Omega}_f, \\
 528 \quad (3.4) \quad \Omega_f^{n+1} &= (\mathbf{I} + \boldsymbol{\eta}_f^{n+1}) \hat{\Omega}_f. \\
 529
 \end{aligned}$$

530

531

We note that in Step 1, the permeability tensor $\boldsymbol{\kappa}^n$ can be a function of the fluid content $\zeta = c_0 p_p + \alpha \nabla \cdot \boldsymbol{\eta}$ in which case

$$\boldsymbol{\kappa}^n = \kappa(c_0 p_p^n + \alpha \nabla \cdot \boldsymbol{\eta}^n) \mathbf{I}.$$

532 The approximations of the solution $(\mathbf{u}_{f,h}^{n+1}, p_{f,h}^{n+1}, \mathbf{u}_{p,h}^{n+1}, p_{p,h}^{n+1}, \boldsymbol{\eta}_h^{n+1}, \dot{\boldsymbol{\eta}}_h^{n+1})$ belong to $V_h^f \times Q_h^f \times$
 533 $V_h^p \times Q_h^p \times X_h^p \times \dot{X}_h^p$, with the corresponding test functions $(\boldsymbol{\phi}_{f,h}, \psi_{f,h}, \boldsymbol{\phi}_{p,h}, \psi_{p,h}, \boldsymbol{\varphi}_{p,h}, \boldsymbol{\xi}_{p,h}) \in$

534 $V_h^f \times Q_h^f \times V_h^p \times Q_h^p \times X_h^p \times \dot{X}_h^p$. We solve the monolithic problem with a preconditioner obtained
 535 using a loosely coupled scheme, as reported in [12].

536 **Stability of the FSI scheme** The focus of this section is on the stability analysis of
 537 method (3.2)-(3.4). As it is often the case, the stability analysis is presented for the linearized
 538 domain motion case (fixed fluid domain), assuming laminar flow and small interface deformation.
 539 In this case, the coupling condition (2.11) reduces to

$$540 \quad (3.5) \quad \mathbf{n} \cdot \boldsymbol{\sigma}_f \mathbf{n} = -p_p \quad \text{on } \hat{\Gamma} \times (0, T).$$

541 We show that our proposed numerical scheme (3.2)-(3.4) written in terms of Nitsche's method
 542 applied to the Navier-Stokes/Biot coupled problem, based on the refactorized Cauchy's ' θ -like'
 543 method, is **unconditionally stable** provided $\theta \in [\frac{1}{2}, 1]$ and the Nitsche penalty parameter γ_f
 544 satisfies a certain condition, made precise in Theorem 3.1 below.

545 To prove the stability estimate, we will be using the following Polarized Identity and the
 546 following Discrete Trace-Inverse Inequality:

547 • Polarized identity:

$$548 \quad (3.6) \quad 2(a - c, b) = a^2 - c^2 - (a - b)^2 + (b - c)^2, \quad \forall a, b, c \in \mathbb{R}.$$

550 • The discrete trace-inverse inequality:

$$551 \quad (3.7) \quad \|\mathbf{D}(\mathbf{u}_h)\mathbf{n}\|_{\hat{\Gamma}}^2 \ll C_{TI} h^{-1} \|\mathbf{D}(\mathbf{u}_h)\|_{\Omega_f}^2,$$

552 where C_{TI} is a positive constant, uniformly bounded from above with respect to the
 553 mesh characteristic size h for a family of shape-regular and quasi-uniform meshes, such
 554 as our domains defined in Sec. 3.1 [41].

555 To analyze the stability of the proposed method, it is convenient to rewrite the linear ex-
 556 trapolations described in Step 2 as a set of forward Euler problems [14]. In particular, Step 2 is
 557 equivalent to the following problem:

558 STEP 2': Given $\mathbf{u}_{f,h}^{n+\theta}, \mathbf{w}^n, \dot{\boldsymbol{\eta}}_h^{n+\theta}, \boldsymbol{\eta}_h^{n+\theta}, p_{p,h}^{n+\theta}$, compute $\mathbf{u}_{f,h}^{n+1}, \dot{\boldsymbol{\eta}}_h^{n+1}, \mathbf{u}_{p,h}^{n+1}, p_{p,h}^{n+1}$, such that

$$559 \quad (3.8) \quad \rho_f \int_{\Omega_f^n} \frac{\mathbf{u}_{f,h}^{n+1} - \mathbf{u}_{f,h}^{n+\theta}}{(1-\theta)\Delta t} \cdot \boldsymbol{\phi}_{f,h} d\mathbf{x} + \rho_f \int_{\Omega_f^n} ((\mathbf{u}_{f,h}^n - \mathbf{w}^n) \cdot \nabla) \mathbf{u}_{f,h}^{n+\theta} \cdot \boldsymbol{\phi}_{f,h} d\mathbf{x}$$

$$560 \quad - \int_{\Omega_f^n} p_{f,h}^{n+\theta} \nabla \cdot \boldsymbol{\phi}_{f,h} d\mathbf{x} + 2\mu_f \int_{\Omega_f^n} \mathbf{D}(\mathbf{u}_{f,h}^{n+\theta}) : \mathbf{D}(\boldsymbol{\phi}_{f,h}) d\mathbf{x}$$

$$561 \quad + \rho_p \int_{\hat{\Omega}_p} \frac{\dot{\boldsymbol{\eta}}_h^{n+1} - \dot{\boldsymbol{\eta}}_h^{n+\theta}}{(1-\theta)\Delta t} \cdot \boldsymbol{\xi}_{p,h} d\mathbf{x} + 2\mu_s \int_{\hat{\Omega}_p} \mathbf{D}(\boldsymbol{\eta}_h^{n+\theta}) : \mathbf{D}(\boldsymbol{\xi}_{p,h}) d\mathbf{x}$$

$$562 \quad + \lambda_p \int_{\hat{\Omega}_p} (\nabla \cdot \boldsymbol{\eta}_h^{n+\theta}) (\nabla \cdot \boldsymbol{\xi}_{p,h}) d\mathbf{x} - \alpha \int_{\hat{\Omega}_p} p_{p,h}^{n+\theta} (\nabla \cdot \boldsymbol{\xi}_{p,h}) d\mathbf{x}$$

$$563 \quad + c_0 \int_{\hat{\Omega}_p} \frac{p_{p,h}^{n+1} - p_{p,h}^{n+\theta}}{(1-\theta)\Delta t} \psi_{p,h} d\mathbf{x} + \alpha \int_{\hat{\Omega}_p} (\nabla \cdot \dot{\boldsymbol{\eta}}_h^{n+\theta}) \psi_{p,h} d\mathbf{x} + \int_{\hat{\Omega}_p} (\nabla \cdot \mathbf{u}_{p,h}^{n+\theta}) \psi_{p,h} d\mathbf{x}$$

$$564 \quad + \int_{\hat{\Omega}_p} (\boldsymbol{\kappa}^n)^{-1} \mathbf{u}_{p,h}^{n+\theta} \cdot \boldsymbol{\phi}_{p,h} d\mathbf{x} - \int_{\hat{\Omega}_p} p_{p,h}^{n+\theta} (\nabla \cdot \boldsymbol{\phi}_{p,h}) d\mathbf{x} - I_h^{*,n+\theta}$$

$$565 \quad = \int_{\Gamma_{in}^f} P_{in}^{n+\theta}(\boldsymbol{\phi}_{f,h} \cdot \mathbf{n}) d\mathbf{S} - \int_{\Gamma_{out}^f} P_{out}^{n+\theta}(\boldsymbol{\phi}_{f,h} \cdot \mathbf{n}) d\mathbf{S}.$$

567 The forward Euler version of Step 2, taking into account the assumptions used in stability
 568 analysis, is used in the following result.

569 THEOREM 3.1. Let C_{TI} be the constant from the discrete trace-inverse inequality (3.7), and
 570 $\varsigma \in \{-1, 0, 1\}$. Furthermore, let the Nitsche's penalty parameter $\gamma_f > 0$ be such that

$$571 \quad \gamma_f > (1 + \varsigma)(\epsilon_f)^{-1}, \text{ where } \epsilon_f < \frac{1}{(1 + \varsigma)C_{TI}}.$$

572 Then the following stability estimate holds:

$$573 \quad (3.9) \quad \begin{aligned} & \frac{\rho_f}{2} \|\mathbf{u}_{f,h}^N\|_{\hat{\Omega}_f}^2 + \frac{\rho_p}{2} \|\dot{\boldsymbol{\eta}}_h^{n+1}\|_{\hat{\Omega}_p}^2 + \frac{c_0}{2} \|p_{p,h}^{n+1}\|_{\hat{\Omega}_p}^2 + \mu_p \|\mathbf{D}(\boldsymbol{\eta}_h^N)\|_{\hat{\Omega}_p}^2 + \frac{\lambda_p}{2} \|\nabla \cdot \boldsymbol{\eta}_h^N\|_{\hat{\Omega}_p}^2 \\ & + (2\theta - 1)\Delta t \sum_{n=0}^{N-1} \|\mathbf{u}_{f,h}^{n+1} - \mathbf{u}_{f,h}^n\|_{\hat{\Omega}_f}^2 + (2\theta - 1)\Delta t \sum_{n=0}^{N-1} \|\dot{\boldsymbol{\eta}}_h^{n+1} - \dot{\boldsymbol{\eta}}_h^n\|_{\hat{\Omega}_p}^2 \\ & + (2\theta - 1)\Delta t \sum_{n=0}^{N-1} \|\boldsymbol{\eta}_h^{n+1} - \boldsymbol{\eta}_h^n\|_{\hat{\Omega}_p}^2 + (2\theta - 1)\Delta t \sum_{n=0}^{N-1} \|p_{p,h}^{n+1} - p_{p,h}^n\|_{\hat{\Omega}_p}^2 \\ & + \mu_f (1 - (1 + \varsigma)\epsilon_f C_{TI}) \Delta t \sum_{n=0}^{N-1} \|\mathbf{D}(\mathbf{u}_{f,h}^{n+\theta})\|_{\hat{\Omega}_f}^2 \\ & + \kappa^{-1} \Delta t \sum_{n=0}^{N-1} \|\mathbf{u}_{p,h}^{n+\theta}\|_{\hat{\Omega}_p}^2 + \beta \Delta t \sum_{n=0}^{N-1} \|(\mathbf{u}_{f,h}^{n+\theta} - \dot{\boldsymbol{\eta}}_h^{n+\theta}) \cdot \mathbf{t}\|_{\hat{\Gamma}}^2 \\ & + \mu_f h^{-1} \Delta t \left(\gamma_f - (1 + \varsigma)\epsilon_f^{-1} \right) \sum_{n=0}^{N-1} \|(\mathbf{u}_{f,h}^{n+\theta} - \mathbf{u}_{p,h}^{n+\theta} - \dot{\boldsymbol{\eta}}_h^{n+\theta}) \cdot \mathbf{n}\|_{\hat{\Gamma}}^2 \\ & \leq \frac{C_T^2 C_P C_K^2}{2\mu_f} \|P_{in}^{n+\theta}\|_{\Gamma_{in}^f}^2 + \frac{C_T^2 C_P C_K^2}{2\mu_f} \|P_{out}^{n+\theta}\|_{\Gamma_{out}^f}^2. \end{aligned}$$

581 *Proof.* To obtain this stability estimate, we start by replacing the test functions in (3.2),
 582 (3.3) by the solutions: $\boldsymbol{\phi}_{f,h} = \mathbf{u}_{f,h}^{n+\theta}$, $\psi_{f,h} = p_{f,h}^{n+\theta}$, $\boldsymbol{\phi}_{p,h} = \mathbf{u}_{p,h}^{n+\theta}$, $\psi_{p,h} = p_{p,h}^{n+\theta}$, $\boldsymbol{\xi}_{p,h} = \dot{\boldsymbol{\eta}}_h^{n+\theta}$ to
 583 obtain:

$$584 \quad (3.10) \quad \begin{aligned} & \frac{\rho_f}{2\theta\Delta t} \left(\|\mathbf{u}_{f,h}^{n+\theta}\|_{\hat{\Omega}_f}^2 + \|\mathbf{u}_{f,h}^{n+\theta} - \mathbf{u}_{f,h}^n\|_{\hat{\Omega}_f}^2 - \|\mathbf{u}_{f,h}^n\|_{\hat{\Omega}_f}^2 \right) + 2\mu_f \|\mathbf{D}(\mathbf{u}_{f,h}^{n+\theta})\|_{\hat{\Omega}_f}^2 \\ & + \frac{\rho_p}{2\theta\Delta t} \left(\|\dot{\boldsymbol{\eta}}_h^{n+\theta}\|_{\hat{\Omega}_p}^2 + \|\dot{\boldsymbol{\eta}}_h^{n+\theta} - \dot{\boldsymbol{\eta}}_h^n\|_{\hat{\Omega}_p}^2 - \|\dot{\boldsymbol{\eta}}_h^n\|_{\hat{\Omega}_p}^2 \right) \\ & + \frac{c_0}{2\theta\Delta t} \left(\|p_{p,h}^{n+\theta}\|_{\hat{\Omega}_p}^2 + \|p_{p,h}^{n+\theta} - p_{p,h}^n\|_{\hat{\Omega}_p}^2 - \|p_{p,h}^n\|_{\hat{\Omega}_p}^2 \right) + \kappa^{-1} \|\mathbf{u}_{p,h}^{n+\theta}\|_{\hat{\Omega}_p}^2 \\ & + \frac{\mu_p}{\theta\Delta t} \left(\|\mathbf{D}(\boldsymbol{\eta}_h^{n+\theta})\|_{\hat{\Omega}_p}^2 - \|\mathbf{D}(\boldsymbol{\eta}_h^n)\|_{\hat{\Omega}_p}^2 + \|\mathbf{D}(\boldsymbol{\eta}_h^{n+\theta}) - \mathbf{D}(\boldsymbol{\eta}_h^n)\|_{\hat{\Omega}_p}^2 \right) \\ & + \frac{\lambda_p}{2\theta\Delta t} \left(\|\nabla \cdot \boldsymbol{\eta}_h^{n+\theta}\|_{\hat{\Omega}_p}^2 - \|\nabla \cdot \boldsymbol{\eta}_h^n\|_{\hat{\Omega}_p}^2 + \|\nabla \cdot \boldsymbol{\eta}_h^{n+\theta} - \nabla \cdot \boldsymbol{\eta}_h^n\|_{\hat{\Omega}_p}^2 \right) \\ & + \beta \|(\mathbf{u}_{f,h}^{n+\theta} - \dot{\boldsymbol{\eta}}_h^{n+\theta}) \cdot \mathbf{t}\|_{\hat{\Gamma}}^2 + \gamma_f \mu_f h^{-1} \|(\mathbf{u}_{f,h}^{n+\theta} - \mathbf{u}_{p,h}^{n+\theta} - \dot{\boldsymbol{\eta}}_h^{n+\theta}) \cdot \mathbf{n}\|_{\hat{\Gamma}}^2 - \mathcal{T} \\ & = \int_{\Gamma_{in}^f} P_{in}^{n+\theta} \mathbf{u}_{f,h}^{n+\theta} \cdot \mathbf{n} d\mathbf{S} - \int_{\Gamma_{out}^f} P_{out}^{n+\theta} \mathbf{u}_{f,h}^{n+\theta} \cdot \mathbf{n} d\mathbf{S}, \end{aligned}$$

592 where

$$593 \quad \mathcal{T} = \int_{\hat{\Gamma}} \mathbf{n} \cdot \boldsymbol{\sigma}_f(\mathbf{u}_{f,h}^{n+\theta}, p_{f,h}^{n+\theta}) \mathbf{n} (\mathbf{u}_{f,h}^{n+\theta} - \mathbf{u}_{p,h}^{n+\theta} - \dot{\boldsymbol{\eta}}_h^{n+\theta}) \cdot \mathbf{n} d\mathbf{S} \\ 594 \quad (3.11) \quad + \int_{\hat{\Gamma}} \mathbf{n} \cdot \boldsymbol{\sigma}_f(\varsigma \mathbf{u}_{f,h}^{n+\theta}, -p_{f,h}^{n+\theta}) \mathbf{n} (\mathbf{u}_{f,h}^{n+\theta} - \mathbf{u}_{p,h}^{n+\theta} - \dot{\boldsymbol{\eta}}_h^{n+\theta}) \cdot \mathbf{n} d\mathbf{S}. \\ 595$$

596 Similarly, we replace the test functions in (3.8) by $\phi_{f,h} = \mathbf{u}_{f,h}^{n+\theta}$, $\psi_{f,h} = p_{f,h}^{n+\theta}$, $\phi_{p,h} = \mathbf{u}_{p,h}^{n+\theta}$, $\psi_{p,h} =$
 597 $p_{p,h}^{n+\theta}$, $\boldsymbol{\xi}_{p,h} = \dot{\boldsymbol{\eta}}_h^{n+\theta}$. We use the polarized identity (3.6) and obtain the following equality:

$$\begin{aligned}
 598 \quad (3.12) \quad & \frac{\rho_f}{2(1-\theta)\Delta t} \left(\|\mathbf{u}_{f,h}^{n+1}\|_{\Omega_f}^2 - \|\mathbf{u}_{f,h}^{n+1} - \mathbf{u}_{f,h}^{n+\theta}\|_{\Omega_f}^2 - \|\mathbf{u}_{f,h}^{n+\theta}\|_{\Omega_f}^2 \right) + 2\mu_f \|\mathbf{D}(\mathbf{u}_{f,h}^{n+\theta})\|_{\Omega_f}^2 \\
 599 \quad & + \frac{\rho_p}{2(1-\theta)\Delta t} \left(\|\dot{\boldsymbol{\eta}}_h^{n+1}\|_{\Omega_p}^2 - \|\dot{\boldsymbol{\eta}}_h^{n+1} - \dot{\boldsymbol{\eta}}_h^{n+\theta}\|_{\Omega_p}^2 - \|\dot{\boldsymbol{\eta}}_h^{n+\theta}\|_{\Omega_p}^2 \right) \\
 600 \quad & + \frac{c_0}{2(1-\theta)\Delta t} \left(\|p_{p,h}^{n+1}\|_{\Omega_p}^2 - \|p_{p,h}^{n+1} - p_{p,h}^{n+\theta}\|_{\Omega_p}^2 - \|p_{p,h}^{n+\theta}\|_{\Omega_p}^2 \right) + \kappa^{-1} \|\mathbf{u}_{p,h}^{n+\theta}\|_{\Omega_p}^2 \\
 601 \quad & + \frac{\mu_p}{(1-\theta)\Delta t} \left(\|\mathbf{D}(\boldsymbol{\eta}_h^{n+1})\|_{\Omega_p}^2 - \|\mathbf{D}(\boldsymbol{\eta}_h^{n+\theta})\|_{\Omega_p}^2 - \|\mathbf{D}(\boldsymbol{\eta}_h^{n+1}) - \mathbf{D}(\boldsymbol{\eta}_h^{n+\theta})\|_{\Omega_p}^2 \right) \\
 602 \quad & + \frac{\lambda_p}{2(1-\theta)\Delta t} \left(\|\nabla \cdot \boldsymbol{\eta}_h^{n+1}\|_{\Omega_p}^2 - \|\nabla \cdot \boldsymbol{\eta}_h^{n+\theta}\|_{\Omega_p}^2 - \|\nabla \cdot \boldsymbol{\eta}_h^{n+1} - \nabla \cdot \boldsymbol{\eta}_h^{n+\theta}\|_{\Omega_p}^2 \right) \\
 603 \quad & + \beta \left((\mathbf{u}_{f,h}^{n+\theta} - \dot{\boldsymbol{\eta}}_h^{n+\theta}) \cdot \mathbf{t} \right)_{\Gamma}^2 + \gamma_f \mu_f h^{-1} \|(\mathbf{u}_{f,h}^{n+\theta} - \mathbf{u}_{p,h}^{n+\theta} - \dot{\boldsymbol{\eta}}_h^{n+\theta}) \cdot \mathbf{n}\|_{\Gamma}^2 - \mathcal{T} \\
 604 \quad & = \int_{\Gamma_{in}^f} P_{in}^{n+\theta} \mathbf{u}_{f,h}^{n+\theta} \cdot \mathbf{n} d\mathbf{S} - \int_{\Gamma_{out}^f} P_{out}^{n+\theta} \mathbf{u}_{f,h}^{n+\theta} \cdot \mathbf{n} d\mathbf{S}. \\
 605
 \end{aligned}$$

606 Multiplying (3.10) by θ and (3.12) by $1 - \theta$, and adding the equations together, we get:

$$\begin{aligned}
 607 \quad (3.13) \quad & \frac{\rho_f}{2\Delta t} \left(\|\mathbf{u}_{f,h}^{n+1}\|_{\Omega_f}^2 - \|\mathbf{u}_{f,h}^{n+1} - \mathbf{u}_{f,h}^{n+\theta}\|_{\Omega_f}^2 + \|\mathbf{u}_{f,h}^{n+\theta} - \mathbf{u}_{f,h}^n\|_{\Omega_f}^2 - \|\mathbf{u}_{f,h}^n\|_{\Omega_f}^2 \right) \\
 608 \quad & + 2\mu_f \|\mathbf{D}(\mathbf{u}_{f,h}^{n+\theta})\|_{\Omega_f}^2 \\
 609 \quad & + \frac{\rho_p}{2\Delta t} \left(\|\dot{\boldsymbol{\eta}}_h^{n+1}\|_{\Omega_p}^2 - \|\dot{\boldsymbol{\eta}}_h^{n+1} - \dot{\boldsymbol{\eta}}_h^{n+\theta}\|_{\Omega_p}^2 + \|\dot{\boldsymbol{\eta}}_h^{n+\theta} - \dot{\boldsymbol{\eta}}_h^n\|_{\Omega_p}^2 - \|\dot{\boldsymbol{\eta}}_h^n\|_{\Omega_p}^2 \right) \\
 610 \quad & + \frac{c_0}{2\Delta t} \left(\|p_{p,h}^{n+1}\|_{\Omega_p}^2 - \|p_{p,h}^{n+1} - p_{p,h}^{n+\theta}\|_{\Omega_p}^2 + \|p_{p,h}^{n+\theta} - p_{p,h}^n\|_{\Omega_p}^2 - \|p_{p,h}^n\|_{\Omega_p}^2 \right) + \kappa^{-1} \|\mathbf{u}_{p,h}^{n+\theta}\|_{\Omega_p}^2 \\
 611 \quad & + \frac{\mu_p}{\Delta t} \left(\|\mathbf{D}(\boldsymbol{\eta}_h^{n+1})\|_{\Omega_p}^2 - \|\mathbf{D}(\boldsymbol{\eta}_h^{n+1}) - \mathbf{D}(\boldsymbol{\eta}_h^{n+\theta})\|_{\Omega_p}^2 + \|\mathbf{D}(\boldsymbol{\eta}_h^{n+\theta}) - \mathbf{D}(\boldsymbol{\eta}_h^n)\|_{\Omega_p}^2 - \|\mathbf{D}(\boldsymbol{\eta}_h^n)\|_{\Omega_p}^2 \right) \\
 612 \quad & + \frac{\lambda_p}{2\Delta t} \left(\|\nabla \cdot \boldsymbol{\eta}_h^{n+1}\|_{\Omega_p}^2 - \|\nabla \cdot \boldsymbol{\eta}_h^{n+1} - \nabla \cdot \boldsymbol{\eta}_h^{n+\theta}\|_{\Omega_p}^2 + \|\nabla \cdot \boldsymbol{\eta}_h^{n+\theta} - \nabla \cdot \boldsymbol{\eta}_h^n\|_{\Omega_p}^2 - \|\nabla \cdot \boldsymbol{\eta}_h^n\|_{\Omega_p}^2 \right) \\
 613 \quad & + \beta \left((\mathbf{u}_{f,h}^{n+\theta} - \dot{\boldsymbol{\eta}}_h^{n+\theta}) \cdot \mathbf{t} \right)_{\Gamma}^2 + \gamma_f \mu_f h^{-1} \|(\mathbf{u}_{f,h}^{n+\theta} - \mathbf{u}_{p,h}^{n+\theta} - \dot{\boldsymbol{\eta}}_h^{n+\theta}) \cdot \mathbf{n}\|_{\Gamma}^2 - \mathcal{T} \\
 614 \quad & = \int_{\Gamma_{in}^f} P_{in}^{n+\theta} \mathbf{u}_{f,h}^{n+\theta} \cdot \mathbf{n} d\mathbf{S} - \int_{\Gamma_{out}^f} P_{out}^{n+\theta} \mathbf{u}_{f,h}^{n+\theta} \cdot \mathbf{n} d\mathbf{S}. \\
 615
 \end{aligned}$$

616 Taking into account the extrapolations defined in Step 2, we have

$$\begin{aligned}
 617 \quad & \|\mathbf{u}_{f,h}^{n+\theta} - \mathbf{u}_{f,h}^n\|_{\Omega_f}^2 - \|\mathbf{u}_{f,h}^{n+1} - \mathbf{u}_{f,h}^{n+\theta}\|_{\Omega_f}^2 = (2\theta - 1) \|\mathbf{u}_{f,h}^{n+1} - \mathbf{u}_{f,h}^n\|_{\Omega_f}^2, \\
 618 \quad & \|\dot{\boldsymbol{\eta}}_h^{n+\theta} - \dot{\boldsymbol{\eta}}_h^n\|_{\Omega_p}^2 - \|\dot{\boldsymbol{\eta}}_h^{n+1} - \dot{\boldsymbol{\eta}}_h^{n+\theta}\|_{\Omega_p}^2 = (2\theta - 1) \|\dot{\boldsymbol{\eta}}_h^{n+1} - \dot{\boldsymbol{\eta}}_h^n\|_{\Omega_p}^2, \\
 619 \quad & \|\boldsymbol{\eta}_h^{n+\theta} - \boldsymbol{\eta}_h^n\|_{\Omega_p}^2 - \|\boldsymbol{\eta}_h^{n+1} - \boldsymbol{\eta}_h^{n+\theta}\|_{\Omega_p}^2 = (2\theta - 1) \|\boldsymbol{\eta}_h^{n+1} - \boldsymbol{\eta}_h^n\|_{\Omega_p}^2, \\
 620 \quad & \|p_{p,h}^{n+\theta} - p_{p,h}^n\|_{\Omega_p}^2 - \|p_{p,h}^{n+1} - p_{p,h}^{n+\theta}\|_{\Omega_p}^2 = (2\theta - 1) \|p_{p,h}^{n+1} - p_{p,h}^n\|_{\Omega_p}^2. \\
 621
 \end{aligned}$$

622 Using the Cauchy-Schwarz inequality and Young's inequality with $\epsilon_f > 0$, we get:

$$\begin{aligned}
 623 \quad & \mathcal{T} \leq 2\mu_f(1 + \varsigma) \|\mathbf{D}(\mathbf{u}_{f,h}^{n+\theta})\mathbf{n}\|_{\Gamma} \|(\mathbf{u}_{f,h}^{n+\theta} - \mathbf{u}_{p,h}^{n+\theta} - \dot{\boldsymbol{\eta}}_h^{n+\theta}) \cdot \mathbf{n}\|_{\Gamma} \\
 624 \quad & \leq \mu_f(1 + \varsigma) \epsilon_f h \|\mathbf{D}(\mathbf{u}_{f,h}^{n+\theta})\|_{\Gamma}^2 + \mu_f(1 + \varsigma) (\epsilon_f h)^{-1} \|(\mathbf{u}_{f,h}^{n+\theta} - \mathbf{u}_{p,h}^{n+\theta} - \dot{\boldsymbol{\eta}}_h^{n+\theta}) \cdot \mathbf{n}\|_{\Gamma}^2. \\
 625
 \end{aligned}$$

626 Applying the discrete trace-inverse inequality (3.7) we obtain:

$$627 \quad \mu_f(1 + \varsigma)\epsilon_f h \|\mathbf{D}(\mathbf{u}_{f,h}^{n+\theta})\|_{\Gamma}^2 \leq \mu_f(1 + \varsigma)\epsilon_f C_{TI} \|\mathbf{D}(\mathbf{u}_{f,h}^{n+\theta})\|_{\Omega_f}^2. \quad 628$$

629 Therefore, the estimate of the boundary term is given by:

$$630 \quad \mathcal{T} \leq \mu_f(1 + \varsigma)\epsilon_f C_{TI} \|\mathbf{D}(\mathbf{u}_{f,h}^{n+\theta})\|_{\Omega_f}^2 + \mu_f(1 + \varsigma)(\epsilon_f h)^{-1} \|(\mathbf{u}_{f,h}^{n+\theta} - \mathbf{u}_{p,h}^{n+\theta} - \dot{\boldsymbol{\eta}}_h^{n+1}) \cdot \mathbf{n}\|_{\Gamma}^2. \quad 631$$

632 To estimate the right hand side of (3.13), we use the Cauchy-Schwarz, Young's, Poincare's and
633 Korn's inequalities to obtain:

$$634 \quad \int_{\Gamma_{in}^f} P_{in}^{n+\theta} \mathbf{u}_{f,h}^{n+\theta} \cdot \mathbf{n} d\mathbf{S} + \int_{\Gamma_{out}^f} P_{out}^{n+\theta} \mathbf{u}_{f,h}^{n+\theta} \cdot \mathbf{n} d\mathbf{S} \\ 635 \quad \leq \|P_{in}^{n+\theta}\|_{\Gamma_{in}^f}^2 \|\mathbf{u}_{f,h}^{n+\theta}\|_{\Gamma_{in}^f}^2 + \|P_{out}^{n+\theta}\|_{\Gamma_{out}^f}^2 \|\mathbf{u}_{f,h}^{n+\theta}\|_{\Gamma_{out}^f}^2 \\ 636 \quad \leq \frac{C_T^2 C_P C_K^2}{2\mu_f} \|P_{in}^{n+\theta}\|_{\Gamma_{in}^f}^2 + \frac{C_T^2 C_P C_K^2}{2\mu_f} \|P_{out}^{n+\theta}\|_{\Gamma_{out}^f}^2 + \mu_f \|\mathbf{D}(\mathbf{u}_{f,h}^{n+\theta})\|_{\Omega_f}^2, \quad 637$$

638 where C_T, C_P and C_K are positive constants. Combining the estimates above with (3.13), multi-
639 plying the results by Δt and calculating the sum from $n = 0$ to $N - 1$, we obtain estimate (3.9). \square

640 Therefore, we have proved (for the fixed fluid domain case) that our proposed numerical
641 scheme (3.2)-(3.4) is unconditionally stable.

642 **3.2. Discretization of the coupled advection-reaction-diffusion problem.** As in the
643 case of the FSI problem above, we use a Finite Element Method-based approach to solve the
644 coupled advection-reaction-diffusion problem (2.22), (2.23) and (2.26). To specify the discretized
645 problem, we must first state the weak formulation of (2.22), (2.23) and (2.26).

Weak formulation. Let us assume that the fluid-structure interface $\Gamma(t)$ is Lipschitz. Fur-
thermore, let $\mathbf{u}_f \in V^f$, and let $\tilde{\mathbf{u}}_p \in L^2(0, T; L^2(\Omega_p(t)))$ be such that $\nabla \cdot \mathbf{u}_p \in L^2(0, T; L^2(\Omega_p(t)))$.
Assume that the domain velocities \mathbf{w}_f and \mathbf{w}_p are such that $\mathbf{w}_f \in L^\infty(0, T; W^{1,\infty}(\Omega_f(t)))$ with
 $\nabla \cdot \mathbf{w}_f \in L^\infty(0, T; W^{1,\infty}(\Omega_f(t)))$, and $\mathbf{w}_p \in L^\infty(0, T; L^2(\Omega_p(t))) \cap L^2(0, T; H^1(\Omega_p(t)))$. We
introduce the following solution space for oxygen concentrations C_f in the fluid channel and C_p
in the hydrogel:

$$\mathcal{C} = \{(C_f, C_p) \in L^2(0, T; H^1(\Omega_f(t))) \times L^2(0, T; H^1(\Omega_p(t))) \mid \\ \partial_t C_f \in L^2(0, T; (H^1(\Omega_f(t)))^*), \partial_t C_p \in L^2(0, T; (H^1(\Omega_p(t)))^*), C_f = C_p \text{ on } \Gamma(t)\}.$$

646 **DEFINITION 3.2.** A function $(C_f, C_p) \in \mathcal{C}$ is said to be a weak solution of the coupled
647 advection-reaction-diffusion problem (2.22), (2.23) and (2.26) if $\forall(\varphi, \psi) \in \mathcal{C}$,

$$648 \quad \int_0^T \int_{\Omega_f(t)} \left\{ \partial_t C_f|_{\mathbf{x}_0} \varphi - \nabla \varphi \cdot [(\mathbf{u}_f - \mathbf{w}_f) C_f - D_f \nabla C_f] + \varphi (\nabla \cdot \mathbf{w}_f) C_f \right\} d\mathbf{x} dt \\ (3.14) \quad + \int_0^T \int_{\Omega_p(t)} \left\{ \partial_t C_p|_{\mathbf{x}_0} \psi - \nabla \psi \cdot [(\tilde{\mathbf{u}}_p - \mathbf{w}_p) C_p - D_p \nabla C_p] + \psi (\nabla \cdot \mathbf{w}_p) C_p \right\} d\mathbf{x} dt \\ = \int_0^T \int_{\Omega_p(t)} R_{\max} \frac{C_p}{C_p + C_{MM}} \delta(C_p > C_{cr}) \psi d\mathbf{x} dt.$$

649 This weak formulation is derived by multiplying equations (2.22), (2.23) by the corresponding
650 test functions, integrating by parts, and using the coupling conditions (2.26) at the fluid structure
651 interface $\Gamma(t)$.

652 **Discretization.** We, again, assume that the shapes of $\Omega_f(t)$ and $\Omega_p(t)$ are polygons/tetrahedra,
 653 and denote by T_h^f and T_h^p the uniform conforming triangulations of $\Omega_f(t)$ and $\Omega_p(t)$, respectively.
 654 We define finite element space $\mathcal{C}_h \subset \mathcal{C}$, and use the Backward Euler method to discretize the
 655 problem in time. The corresponding fully discretized coupled problem for oxygen concentration
 656 reads:

$$\begin{aligned}
 657 \quad & \int_{\Omega_f^n} \left\{ \frac{C_{f,h}^{n+1} - C_{f,h}^n}{\Delta t} \Big|_{\mathbf{x}_0} \varphi_h - \nabla \varphi_h \cdot [(\mathbf{u}_{f,h}^n - \mathbf{w}_{f,h}^n) C_{f,h}^{n+1} - D_f \nabla C_{f,h}^{n+1}] + \varphi_h (\nabla \cdot \mathbf{w}_{f,h}^n) C_{f,h}^{n+1} \right\} d\mathbf{x} \\
 658 \quad & + \int_{\Omega_p^n} \left\{ \frac{C_{p,h}^{n+1} - C_{p,h}^n}{\Delta t} \Big|_{\mathbf{x}_0} \psi_h - \nabla \psi_h \cdot [(\tilde{\mathbf{u}}_{p,h}^n - \mathbf{w}_{p,h}^n) C_{p,h}^{n+1} - D_p \nabla C_{p,h}^{n+1}] + \psi_h (\nabla \cdot \mathbf{w}_{p,h}^n) C_{p,h}^{n+1} \right\} d\mathbf{x} \\
 659 \quad & = \int_{\Omega_p^n} \left(R_{\max} \frac{C_{p,h}^n}{C_{p,h}^n + C_{MM}} \delta(C_{p,h}^n > C_{cr}) \right) \psi_h d\mathbf{x}, \\
 660
 \end{aligned}$$

661 where $(C_{f,h}^{n+1}, C_{p,h}^{n+1}) \in \mathcal{C}_h$, and $(\varphi_h, \psi_h) \in \mathcal{C}_h$.

662 **3.3. Parameter estimation using Encoder-Decoder Convolution Neural Networks**
 663 **and Smoothed Particle Hydrodynamics.** Local information about hydraulic permeability of
 664 the 3D islet chamber is crucial for correctly approximating oxygen supply to the pancreatic islets
 665 seeded in the chamber containing a gel poroelastic matrix. While **global** hydraulic permeability
 666 can be estimated using experiments, the **local** properties are difficult to obtain experimentally.
 667 This is why we use our in-house Smoothed Particle Hydrodynamics (SPH) solver, developed
 668 based on the works [32, 33, 31], and experimentally validated in [43], to estimate the values of
 669 equilibrium permeability κ_0 from (2.4) at every point (x, y, z) in the poroelastic hydrogel. To
 670 achieve equilibrium permeability, constant pressure drop is prescribed at the inlet and outlet.

671 The SPH is a weighted interpolation method which represents all bulk properties of the fluid
 672 at a certain location in space with a discrete interpolation over a set of surrounding particles
 673 [32, 33, 31, 43]. The particles corresponding to the hydrogel matrix are fixed in a random fashion
 674 over the hydrogel domain, satisfying a certain porosity volume fraction condition, while the
 675 moving particles describing the fluid satisfy a system of differential equations corresponding to
 676 the Navier-Stokes/Stokes equations. The ratio between the fixed particles and moving particles
 677 is given a priori, and it corresponds to the porosity of the hydrogel. At the inlet and outlet of the
 678 domain, the particles are leaving and entering the domain so that for every exiting particle, there
 679 is a new particle assigned at the inlet, with a given inlet velocity. A result of one such simulation
 680 is shown in Fig. 8: we see a 2D slice of a 3D hydrogel where the inlet is on the left, and the outlet
 681 on the right. The first two panels in this figure show the magnitude of fluid/plasma filtration
 682 velocity and pressure, respectively. The last two panels on this figure show the permeability
 683 coefficients $[\kappa_0]_{11}$ and $[\kappa_0]_{33}$ obtained by locally applying Darcy law.

684 Since 3D SPH simulations are computationally expensive to be run for every single hydrogel
 685 geometry, we resort to the Encoder-Decoder Convolution Neural Networks (CNN), see e.g. [29,
 686 34, 4], to obtain the macro-scale permeability tensor, based on the micro-scale hydrogel geometry.
 687 We use synthetic data from the SPH simulations to train the network and obtain a macro-scale
 688 permeability tensor as a function of (x, y, z) for either synthetic/numerically generated hydrogels,
 689 or for the actual hydrogels whose geometry is obtained from imaging data.

690 The main idea behind the Encoder-Decoder Neural Network applied to our problem is based
 691 on treating the geometry of the gel poroelastic matrix as the input, and train the Encoder-
 692 decoder based CNN over a large set of synthetic data obtained using our pre-validated steady
 693 state simulations, to estimate the local hydraulic permeability tensor κ_0 as an output of the
 694 CNN. The main steps are as follows:

695 1. **Create an ensemble** of 100 poroelastic gel matrix geometries with different porosity by
 696 using SPH to distribute the solid particles in the hydrogel. The hydrogel is divided into boxes

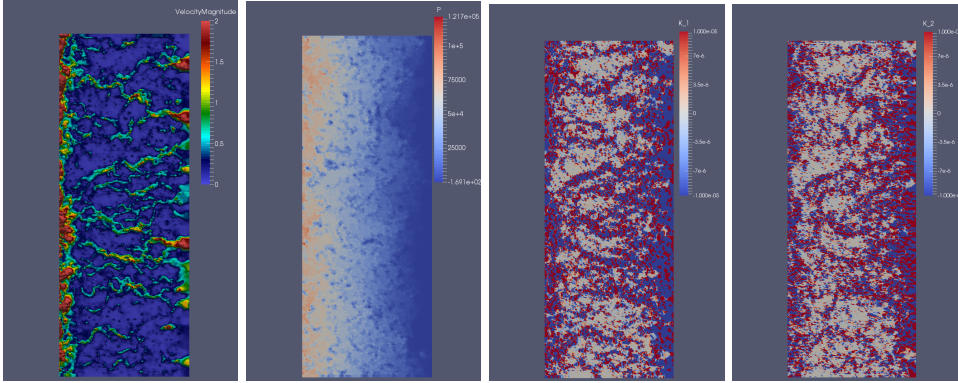


FIG. 8. A SPH simulation of a 2D slice of a synthetically generated hydrogel showing: (a) Filtration velocity magnitude ; (b) Pressure field; (c) Hydraulic conductivity coefficient in horizontal direction $[\kappa_0]_{11}$, and (d) in vertical direction $[\kappa_0]_{33}$.

697 and treated as an image. Every box (cf. pixel) contains the information about the density of the
 698 non-moving SPH particles in that box (cf. pixel intensity in terms of image processing).

699 **2. Run SPH simulations** for each poroelastic matrix geometry to obtain the corresponding
 700 filtration flow and pressure, as illustrated in Fig. 8(a) and (b).

701 **3. Post-processing:** At each location in the chamber, compute the local hydraulic perme-
 702 ability tensor using data from step 2 above, see Fig. 8(c) and (d), and use it as training data
 703 (permeability map) for the Encoder-Decoder CNN.

704 **4. Train the Encoder-Decoder CNN** with the density data and corresponding perme-
 705 ability map obtained from steps 2 and 3. We use TensorFlow as our platform. The encoder
 706 contains several Convolution and Dense layers, and the decoder is just the reflection of those
 707 layers in the encoder.

708 **5. Feed** a new density matrix to the Encoder-decoder CNN and predict the local values of
 709 the hydraulic conductivity tensor for a new porous medium chamber.

710 While CNN training is an expensive part of this approach, it is performed “off-line” and
 711 only once. Once this is completed, getting new parameter values for different poroelastic matrix
 712 geometries is fast, and does not require the expensive SPH simulations. This approach is signif-
 713 icantly “cheaper” computationally than generating and running new SPH simulations each time
 714 a new islet geometry is to be tested.

715 **3.4. Parallel implementation and convergence test.** Our macro-scale solvers have
 716 been implemented within the FEniCS platform [20]. The macro-scale solvers, and the the nano-
 717 scale SPH solver, have both been **parallelized**. The nano-scale SPH solver has been running
 718 on a GPU node on the Savio cluster at UC Berkeley. Each GPU node is equipped with two
 719 Nvidia K80 GPU cards, where each card can run up to 2496 CUDA cores. One typical SPH
 720 simulation uses one whole node with a total of 2496 cores. The FSI solver has been running on
 721 the General Savio node pool. Each node is equipped with two Intel Xeon 12 core processors and
 722 128 GB memory. We use 8 cores on each node, with 16 allocated nodes. We get nearly linear
 723 speedup for our solver implemented in FEniCS before reaching the memory limit for each node.
 724 FEniCS parallelization is different from the traditional approaches as it runs N identical copies
 725 of code in parallel, where N refers to the number of cores, and the original problem is divided
 726 into N subproblems. There is no master node to manage running the job, and each individual
 727 core executes its own job with gathering only the information it needs.

Convergence test of the FSI θ -scheme. We conclude this section by showing that our proposed one legged ‘ θ – like’ method for the FSI problem, presented in Sec. 3.1, has higher order accuracy than the currently available Navier-Stokes-Biot schemes reported in [12, 42]. In our convergence test, as stated above at the beginning of Sec. 2.1, we assume the thick poroelastic structure to be homogeneous and isotropic, and the stress tensor to be given by the first Piola-Kirchhoff stress tensor: $\Sigma(\mathbf{d}) = 2\mu_s\epsilon(\mathbf{d}) + \lambda_s(\nabla \cdot \mathbf{d})\mathbf{I}$, where $\epsilon(\mathbf{d}) = \frac{\nabla\mathbf{d}+(\nabla\mathbf{d})^T}{2}$ is the strain rate tensor, μ_s and λ_s are the Lamé constants, which are related to Young’s modulus E_s and the Poisson’s ratio ν_s via:

$$\mu_s = \frac{E_s}{2 + 2\nu_s}, \quad \lambda_s = \frac{E_s\nu_s}{(1 + \nu_s)(1 - 2\nu_s)}.$$

728 We solve our FSI problem using the *method of manufactured solutions*, which were derived
729 assuming that the fluid domain remains fixed during the simulation. The computational domain
730 consists of a unit cube, where the top part of the cube corresponds to the fluid and the bottom
731 part corresponds to the poroelastic structure, i.e., $\hat{\Omega}_f = (0, 1) \times (0, 1) \times (0, 0.5)$ and $\hat{\Omega}_p =$
732 $(0, 1) \times (0, 1) \times (-0.5, 0)$. The exact solution is given by:

$$\begin{aligned} 733 \quad \boldsymbol{\eta}_{ref} &= \begin{bmatrix} \sin(\pi t)(\cos(y) - 3x) \\ \sin(\pi t)(y + 1) \\ \frac{2}{3}\sin(\pi t)z \end{bmatrix}, \\ 734 \quad p_{p,ref} &= \sin\left(\pi t + \frac{\pi}{4}\right)\sin(\pi x)\cos(0.5\pi y) - \frac{4}{3}\pi\cos(\pi t), \\ 735 \quad \mathbf{u}_{f,ref} &= \begin{bmatrix} \pi\cos(\pi t)(\cos(y) - 3x) \\ \pi\cos(\pi t)(y + 1) \\ \frac{2}{3}\pi\cos(\pi t)z \end{bmatrix}, \quad p_{f,ref} = \sin\left(\pi t + \frac{\pi}{4}\right)\sin(\pi x)\cos(0.5\pi y). \\ 736 \end{aligned}$$

Forcing terms, $\mathbf{u}_{p,ref}$ and $\dot{\boldsymbol{\eta}}_{ref}$, as well as the boundary conditions, are computed using the exact solution. We note that the exact velocity is not divergence-free, in which case we also add a forcing term to the mass conservation equation:

$$\nabla \cdot \mathbf{u}_f = F_m,$$

737 where F_m is computed using the exact solution. We impose the following boundary conditions

$$\begin{aligned} 738 \quad \mathbf{u}_f &= \mathbf{u}_{f,ref} && \text{on } \partial\hat{\Omega}_p \setminus (\hat{\Gamma} \cup \hat{\Gamma}^*), \\ 739 \quad \boldsymbol{\sigma}_f(\mathbf{u}_f, p_f)\mathbf{n} &= \boldsymbol{\sigma}_f(\mathbf{u}_{f,ref}, p_{f,ref})\mathbf{n} && \text{on } \hat{\Gamma}^*, \\ 740 \quad \boldsymbol{\eta}_f &= \boldsymbol{\eta}_{f,ref} && \text{on } \partial\hat{\Omega}_p \setminus \hat{\Gamma}, \\ 741 \quad p_p &= p_{p,ref} && \text{on } \partial\hat{\Omega}_p \setminus \hat{\Gamma}, \end{aligned}$$

743 where $\hat{\Gamma}^*$ is the fluid external boundary corresponding to the plane $x = 0$. The parameter values
744 used in this simulation are all set to one: $\rho_f = \mu_f = \rho_p = \mu_s = \lambda_s = \alpha = c_0 = \beta = 1$ and $\boldsymbol{\kappa}$ is
745 equal to the identity matrix. We use $\theta = 0.5 + \Delta t$, $\gamma_f = 10^4$, and the final time is set to $T = 0.2$.
746 In this case, a second-order convergence is expected.

Our convergence test was conducted on a fixed domain, where the mesh was refined together with the time step. In particular, the following temporal and spatial parameters are used:

$$(\Delta t, h) = \left\{ \frac{4 \cdot 10^{-2}}{2^i}, \frac{0.5}{2^i} \right\}_{i=0}^2.$$

747 We use $\mathbb{P}_2 - \mathbb{P}_1$ elements for the fluid velocity and pressure, \mathbb{P}_2 elements for the structure dis-
748 placement, and $\mathbb{P}_2 - \mathbb{P}_1$ elements for the filtration velocity and porous pressure. We compute the

749 relative errors for $\mathbf{u}_f, p_f, \mathbf{u}_p, p_p, \boldsymbol{\eta}, \boldsymbol{\xi}$, defined by

$$750 \quad \mathbf{e}_k = \frac{\|\mathbf{u}_k - \mathbf{u}_{k,ref}\|_{L^2(\hat{\Omega}_k)}}{\|\mathbf{u}_{k,ref}\|_{L^2(\hat{\Omega}_k)}}, \quad e_{p,k} = \frac{\|p_k - p_{k,ref}\|_{L^2(\hat{\Omega}_k)}}{\|p_{k,ref}\|_{L^2(\hat{\Omega}_k)}}, \quad k = f, p,$$

$$751 \quad \mathbf{e}_\boldsymbol{\eta} = \frac{\|\boldsymbol{\eta} - \boldsymbol{\eta}_{ref}\|_S}{\|\boldsymbol{\eta}_{ref}\|_S}, \quad \mathbf{e}_{\dot{\boldsymbol{\eta}}} = \frac{\|\dot{\boldsymbol{\eta}} - \dot{\boldsymbol{\eta}}_{ref}\|_{L^2(\hat{\Omega}_p)}}{\|\dot{\boldsymbol{\eta}}_{ref}\|_{L^2(\hat{\Omega}_p)}},$$

752

where $\|\cdot\|_S$ is the structure energy norm defined by

$$\|\boldsymbol{\eta}\|_S^2 = 2\mu_S \|\mathbf{D}(\boldsymbol{\eta})\|_{L^2(\hat{\Omega}_p)}^2 + \lambda_S \|\nabla \cdot \boldsymbol{\eta}\|_{L^2(\hat{\Omega}_p)}^2.$$

The results are reported in Tables 3 and 4. This shows that our one legged ‘ θ -like’ scheme is

Δt	\mathbf{e}_f	rate	$e_{p,f}$	rate	\mathbf{e}_p	rate
$4 \cdot 10^{-2}$	$2.5 \cdot 10^{-3}$	-	$1.2 \cdot 10^{-1}$	-	0.3127	-
$2 \cdot 10^{-2}$	$3.6 \cdot 10^{-4}$	2.78	$2.8 \cdot 10^{-2}$	2.11	0.0707295	2.14
$1 \cdot 10^{-2}$	$9.1 \cdot 10^{-5}$	1.99	$1.4 \cdot 10^{-2}$	0.96	0.0252249	1.49

TABLE 3
Temporal convergence test for variables \mathbf{u}_f, p_f , and \mathbf{u}_p .

Δt	$e_{p,p}$	rate	$\mathbf{e}_\boldsymbol{\eta}$	rate	$\mathbf{e}_{\dot{\boldsymbol{\eta}}}$	rate
$4 \cdot 10^{-2}$	$1.0 \cdot 10^{-2}$	-	$3.1 \cdot 10^{-3}$	-	$2.6 \cdot 10^{-3}$	-
$2 \cdot 10^{-2}$	$2.5 \cdot 10^{-3}$	2.16	$6.9 \cdot 10^{-4}$	2.16	$5.7 \cdot 10^{-4}$	2.05
$1 \cdot 10^{-2}$	$5.9 \cdot 10^{-4}$	1.92	$1.8 \cdot 10^{-4}$	1.92	$1.5 \cdot 10^{-4}$	2.07

TABLE 4
Temporal convergence test for variables $p_p, \boldsymbol{\eta}$ and $\dot{\boldsymbol{\eta}}$.

753
754 second-order accurate for the fluid velocity, structure displacement and velocity, and filtration
755 pressure, and therefore has higher-order accuracy than other Navier-Stokes-Biot schemes reported
756 in [12, 42], which are only first-order accuracy in time.

757 **4. Numerical results.** We study numerically the current prototype of the bioartificial
758 pancreas, shown in Figs. 4 and 5, and propose modifications in the design that promise to lead
759 to increased filtration flow and increased oxygen concentration.

760 Tables 1 and 2 show the parameter values used in the simulations. The initial and boundary
761 conditions are specified in Sec. 2.

762 **4.1. One outlet – current prototype design.** We start by considering the design shown
763 in Fig. 4. As mentioned above, in this design one outlet is associated with the outlet gasket. A
764 detailed computational domain showing the outlet cylinder, the top gasket, the islet chamber with
765 drilled ultrafiltrate channels, the bottom gasket and the four inlet nano-pore size membranes (the
766 four squares at the bottom of the chamber) is shown in Fig. 9 top. Fig. 9 bottom shows filtration
767 flow streamlines with the colors denoting magnitude of filtration velocity. Red denotes high and
768 blue low filtration velocity. As expected, the filtration velocity at the inlet and near the inlet
769 at the bottom gasket is high. The flow then enters the islet chamber both via the ultrafiltrate
770 channels and also through the poroelastic hydrogel away from the channels. We see high velocity
771 at the bottom of the islet chamber adjacent to the gasket-hydrogel interface, showing strong
772 filtrate flow everywhere. As we move up further away from the bottom gasket, the filtrate flow is

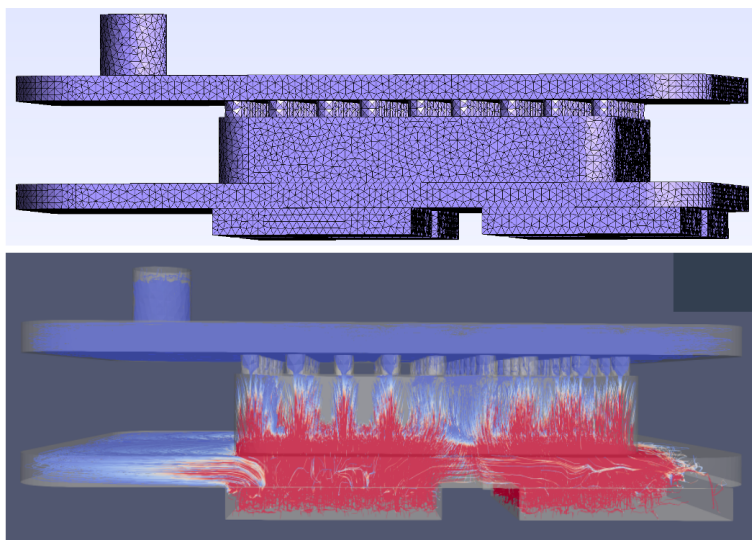


FIG. 9. Computational domain and streamlines corresponding to the red box in Fig. 4. The inlet is at the bottom through four membranes, and the outlet is at the top through the vertical cylinder. The maximal velocity is 3.5 cm/s (shown in red).

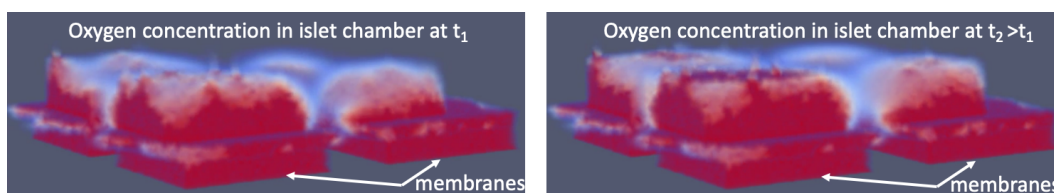


FIG. 10. Oxygen concentration at the membranes (inlet) and within the islet chamber for two different times t_1 and $t_2 > t_1$ as the initial oxygen front convected with the flow enters the bioartificial pancreas. Red denotes high concentration and white and blue low concentration. The flow is from bottom to top. We can see that the regions on the left in both pictures, which are closest to the outlet, get more oxygen than the regions on the right.

773 diminished, and most flow takes place through the ultrafiltrate channels. It is therefore expected
 774 that oxygen concentration would be greatest near the inlet to the islet chamber and close to the
 775 ultrafiltrate channels, rather than near the outlet of the chamber.

776 Indeed Fig. 10 shows oxygen concentration at two different times t_1 and $t_2 > t_1$. We see
 777 how oxygen populates the islet chamber, with red denoting high oxygen concentration, blue low
 778 oxygen concentration, and white intermediate oxygen concentration.

779 One can observe high oxygen concentration at the inlet membranes, in the gasket close to
 780 the islet chamber, and in much of the islet chamber, with highest oxygen concentration closer to
 781 the inlet. Furthermore, when comparing the left “half” of the chamber, which is closest to the
 782 outlet, we see that it has higher oxygen concentration than the right “half” of the chamber. We
 783 attribute this to the larger bulk flow closer to the outlet.

784 In fact, to investigate this situation further, we simulated the flow in the entire set up, as
 785 shown in Fig. 11, with six semi-permeable nanopore membranes and flow through the ultrafiltrate
 786 channels, as shown in Fig. 11 top. The top gasket collects all the outflow which leaves the device
 787 through one ultrafiltrate outlet. As shown in Fig. 11 top, the bulk of the flow occurs through
 788 the membranes/islet chambers closest to the outlet (the first three membranes closest to the
 789 outlet). Here red denotes high flow and blue low flow, as before. We conclude that adding

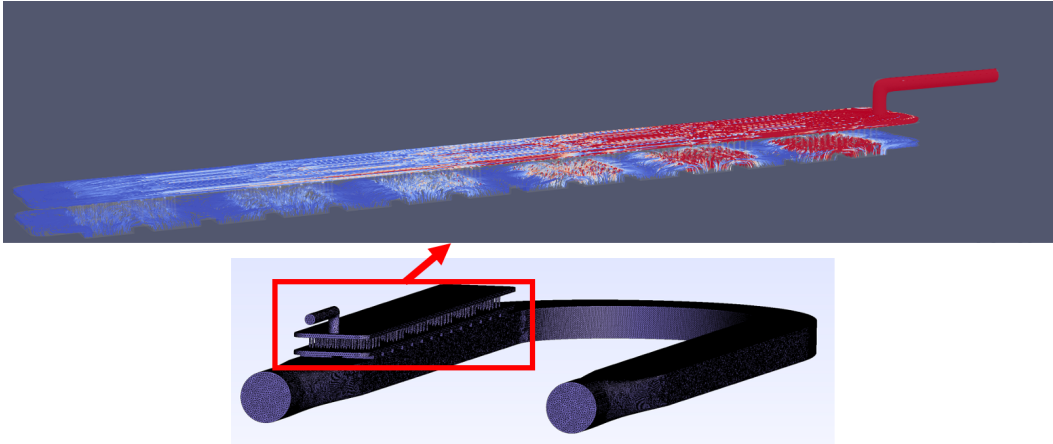


FIG. 11. Entire loop. Top: The colors denote the magnitude of fluid velocity with red denoting high velocity (maximum velocity is equal to 3.5 cm/s) and blue denoting low velocity (minimum velocity is 0 cm/s). Bottom: The entire computational domain with mesh.

790 several additional outlets to the top gasket would improve filtration flow everywhere within the
 791 islet chamber situated between the membranes and the top gasket. This is investigated next.

792 **4.2. Two outlets versus one outlet.** Here we investigate the influence of two outlets in
 the design shown in Fig. 12 top, on filtration flow and oxygen concentration. Fig. 12 top shows

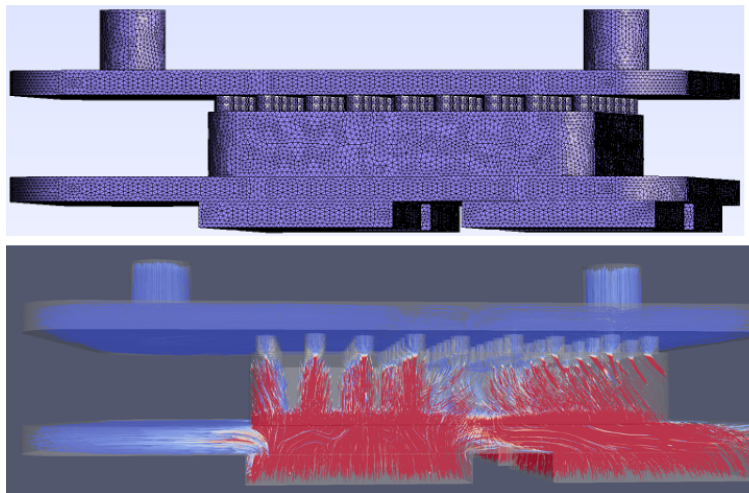


FIG. 12. Computational domain and velocity streamlines for the case with two outlets. The maximum velocity is between 3.4 cm/s.

793 the computational domain, and Fig. 12 bottom shows the filtration velocity streamlines, with
 794 colors corresponding to the velocity magnitude. Two interesting observations can be made from
 795 the results in Fig. 12:
 796

- 797 • The presence of the second outlet improves the flow through the part of the islet chamber
 798 closest to that outlet (see Fig. 12 right).
- 799 • The staggered distribution of islet chamber and membranes underneath the chamber,
 800 increases transverse flow through the islet chamber. This is shown by the angled stream-

801 lines in Fig. 12 right.

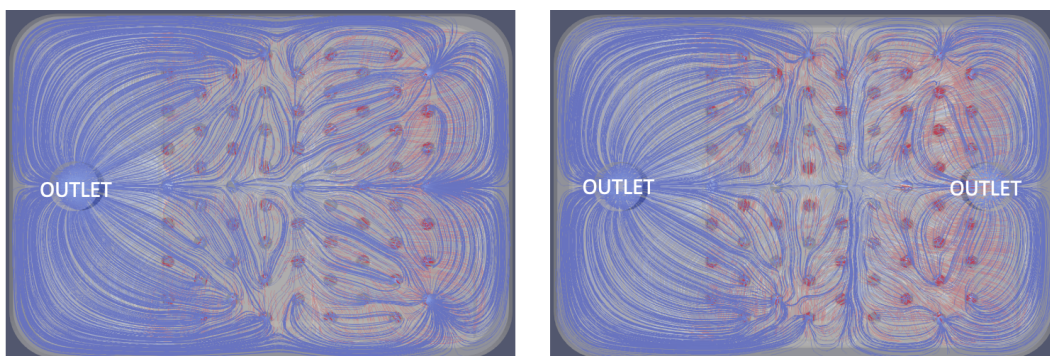


FIG. 13. Comparison of the streamlines viewed from the top for the designs with one outlet (left), c.f. Fig. 9, and with two outlets (right), c.f. Fig. 12. The top view shows the outlets, the slow flow (blue) in the top gasket, and the faster flow (red) in the islet chamber. The same velocity scale was used for both pictures. We see stronger flow through the islet chamber on the right (two outlets). In particular, the transverse flow, away from the ultrafiltrate channels, is much stronger in the case of two outlets. This can also be seen in Fig. 12(bottom). A combination of the presence of the second outlet and the “misalignment between the islet chamber and the two inlet membranes in the right half of the chamber is responsible for the increase in transverse (diagonal) flow.

802 Increased transverse flow through the islet chamber away from the ultrafiltrate channels can also
 803 be seen in Fig. 13. Fig. 13 shows a view from the top at two device designs: the one on the
 804 left has one outlet, the one on the right has two outlets. We can see an increase in transverse
 805 (diagonal) flow through the islet chamber, shown with red streamlines, in the design with two
 806 outlets. A combination of the presence of the second outlet and the “misalignment between the
 807 islet chamber and the two inlet membranes in the right half of the chamber is responsible for the
 808 increase in transverse (diagonal) flow.

809 The presence of the second outlet also helps avoid recirculation zones in the top gasket.
 810 Recirculation zones can be seen in Fig. 13 left where the right-half of the top gasket shows areas
 811 of recirculation flow. This is even more pronounced in Fig. 14 where a large recirculation zone
 in the top gasket away from the outlet can be seen.

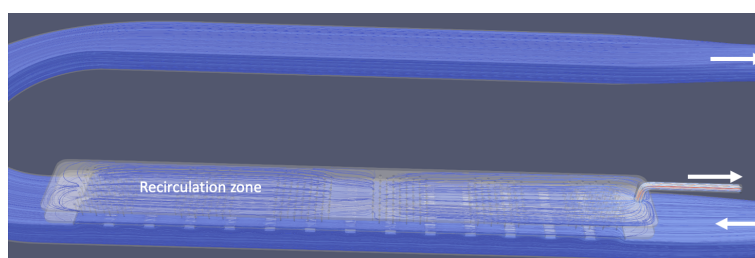


FIG. 14. Large recirculation zone in device design with only one outlet.

812 We further investigated the influence of two outlets on oxygen concentration in the islet
 813 chamber. Fig. 15 shows a comparison in oxygen concentration between the two designs. The
 814 figure on the left corresponds to the design with one outlet, and the figure on the right corresponds
 815 to the design with two outlets. One can see that the design with two outlets shown on the right
 816 has larger regions with high oxygen concentration, as well as larger regions with dark red color
 817 indicating higher oxygen concentration.
 818

819 To obtain more detailed information about oxygen concentration in the design with two

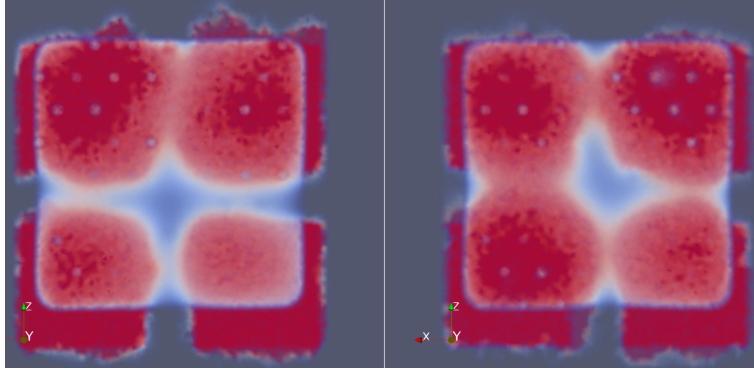


FIG. 15. Comparison of oxygen concentration viewed from the top for the designs with one outlet (left), c.f. Fig. 9, and with two outlets (right), c.f. Fig. 12. The same concentration scale was used for both pictures. High oxygen concentration is shown in red, and low in white and blue. We see larger regions of high oxygen concentration in the figure on the right, corresponding to the design with two outlets. The purple dots are the outlines of the ultrafiltrate channels.

outlets, we present a 2D slice through a 3D islet chamber, shown in Figs. 16 and 17. Fig. 16

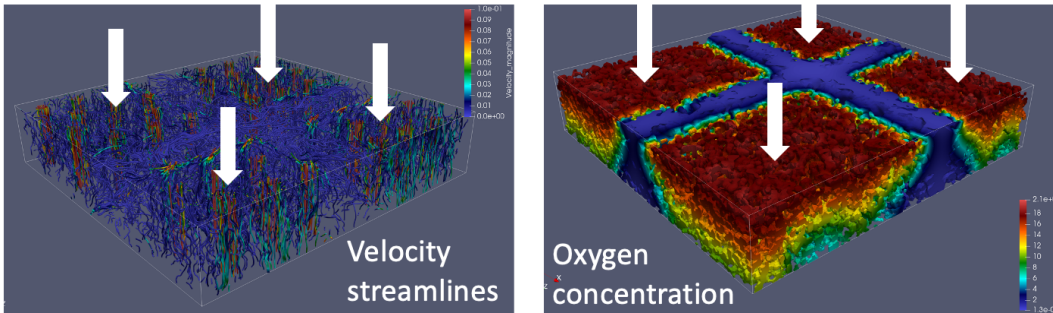


FIG. 16. Velocity streamlines colored by velocity magnitude (left), and oxygen concentration (right) in the poroelastic gel. The direction of flow is from top to bottom. The red streamlines in the figure on the right indicate where the ultrafiltrate channels are located.

820 left shows the islet chamber with flow streamlines, with the flow entering the chamber from the
 821 top, and leaving at the bottom. On the right we see the corresponding oxygen concentration
 822 distributed within the chamber. Red is high, and dark blue low oxygen concentration, with the
 823 maximum concentration equal to $1.06 \times 10^{-7} \text{ mol/cm}^3$. Fig. 17 shows a 2D slice through the
 824 3D islet chamber. We see, again, that high oxygen concentration occurs near the inlet, and close
 825 to the filtration channels (red drop-like vertical structures). The dark blue region where oxygen
 826 concentration is low corresponds to the area just under the frame of the membranes where there
 827 is no filtration flow entering the islet chamber. In both figures the flow comes from the top and
 828 leaves the islet chamber at the bottom.
 829

830 **4.3. Hydrogel elasticity.** Finally, we investigate the influence of hydrogel elasticity on
 831 flow and oxygen concentration. This is particularly important since elasticity can be controlled
 832 in the fabrication of agarose hydrogel scaffolds, fabricated using the approaches presented in
 833 [37]. Hydrogel elasticity is directly related to cells viability [1]. To investigate the influence of
 834 hydrogel elasticity on flow and oxygen concentration we performed two simulations: one assumes
 835 poroelasticity of a hydrogel, as described by the Biot model in Sec. 2.1, and the other assumes that

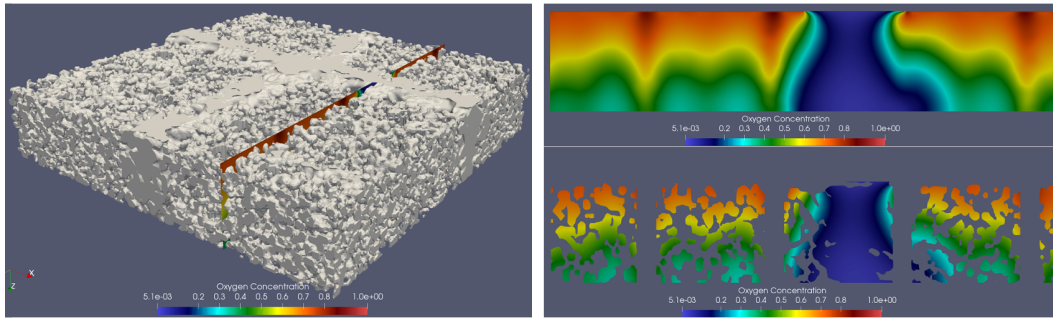


FIG. 17. Detailed information about oxygen concentration within the hydrogel for the case with two outlets. Left: 3D hydrogel with a 2D slice. Right: A section of the 2D slice through hydrogel containing details of oxygen concentration (top) and hydrogel structure (bottom). Red is high oxygen concentration and dark blue is low oxygen concentration. Maximum oxygen concentration was $1.06 \times 10^{-7} \text{ mol/cm}^3$. The flow is from top to bottom. The dark red colors with high concentration indicate where the ultrafiltrate channels are located.

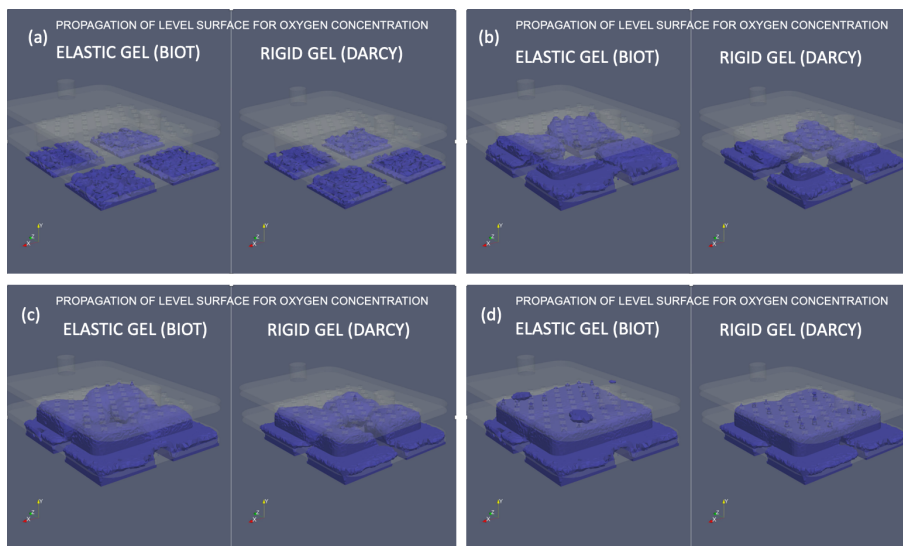


FIG. 18. Oxygen front propagation: Comparison between the Biot model (assuming poroelastic hydrogel), and Darcy model (assuming rigid porous hydrogel). The figure shows four snapshots at increasing times from (a)-(d) showing the propagation of a level surface of oxygen concentration. In figure (d) we see that oxygen front has already reached the top gasket in the case of the poroelastic Biot model (figure (d) left), while in the case of the rigid gel modeled by Darcy law, the front is still within the islet chamber, not yet reaching the top gasket (figure (d) right).

836 hydrogels are rigid, and uses Darcy equation to calculate filtration flow through the hydrogel. We
 837 found that hydrogel elasticity improves both filtration flow and oxygen concentration within the
 838 hydrogel. Fig. 18 shows the propagation of oxygen front (a level surface of oxygen concentration)
 839 as a function of time. The four panels in this figure show four snapshots of oxygen front
 840 propagation increasing in time from (a) to (d). Indeed, one can see that in the case of a poroelastic
 841 hydrogel, shown on the left in each of the four panels, oxygen front travels faster, and reaches
 842 the top gasket before the oxygen front in the rigid hydrogel, shown on the right in each of
 843 the four figures. Thus, elasticity of a hydrogel seems to be conducive to increased filtration
 844 flow, c.f. Fig. 19 below, and faster oxygenation of the islet chamber. We further investigated the

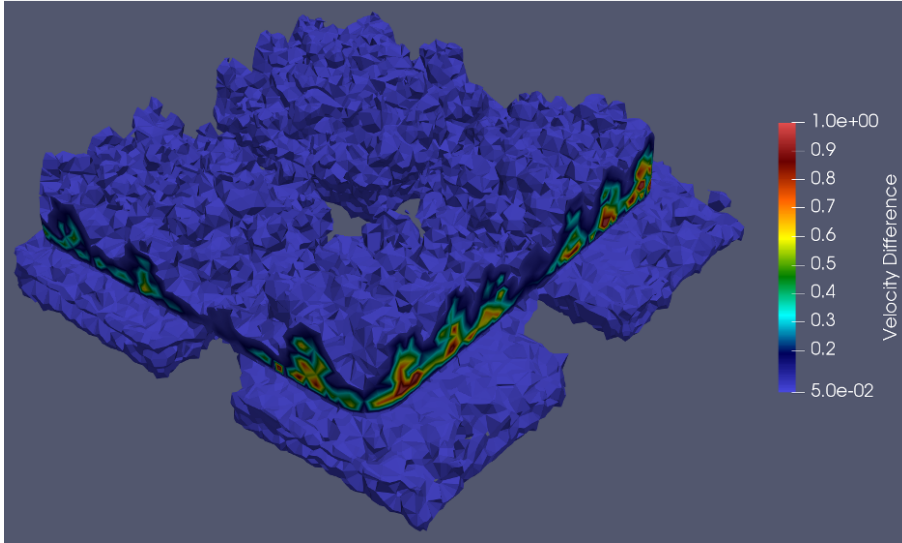


FIG. 19. Difference in velocity magnitude between filtration flow through an poroelastic hydrogel, modeled by the Biot model, and rigid hydrogel, modeled by Darcy law. Red is high and blue is low velocity difference. Biot filtration velocity has a higher magnitude, indicating that hydrogel elasticity is conducive to increased filtration flow.

845 filtration velocity for the two cases, Biot versus Darcy, and found that indeed, there is a significant
 846 difference in filtration velocity between the two models. While the maximum velocity occurs for
 847 the Biot model and is equal to 3.5 cm/s, the maximum difference in the two velocities is 1 cm/s,
 848 which is almost one third of the maximal filtration velocity. We attribute this difference to the
 849 fluid pressure-related swelling of the hydrogel pores, accommodating more fluid, especially near
 850 the inlet into the hydrogel region. The difference between the filtration fluid velocity between
 851 the two scenarios is shown in Fig. 19.

852 We conclude this section by comparing the overall oxygen concentration within three hydro-
 853 gels with three different elastic moduli: alginate hydrogel with Youngs modulus $E = 4 \times 10^4$
 854 Pascals, alginate with $E = 0.75 \times 10^6$ Pa, and a very stiff scaffold made of Polycaprolactone
 855 (PCL) with $E = 1.3 \times 10^8$ Pa. All the other properties, such as porosity and permeability, were
 856 assumed to be the same. Fig. 20 shows three curves of oxygen concentration over time, one for
 857 each cell scaffold. We see that there is a significant increase in oxygen concentration within the
 858 elastic alginate scaffolds with Youngs moduli $E = 4 \times 10^4$ Pa and $E = 0.75 \times 10^6$, in compari-
 859 son with the stiff Polycaprolactone (PCL) scaffold with $E = 1.3 \times 10^8$ Pa modeled using Darcy
 860 model. Fig. 20 shows that oxygen concentration in the most elastic scaffold, namely alginate
 861 gel with $E = 4 \times 10^4$ P, is 30% higher than that in the stiffest scaffold considered in this study.
 862 This is particularly interesting considering that scaffold elasticity can be controlled during their
 863 fabrication, and that elastic scaffolds improve cell viability [1].

864 **5. Conclusions.** We developed a multi-scale mathematical and computational model to
 865 study cell encapsulation and design of an implantable bioartificial pancreas (iBAP). The macro-
 866 scale models include a fluid-structure interaction (FSI) model describing the flow of blood plasma
 867 through a poroelastic hydrogel, and a set of two coupled advection-reaction-diffusion models
 868 defined on moving domains: the hydrogel and two gaskets adjacent to the hydrogel. A novel
 869 second-order accurate finite element numerical scheme was designed to solve the FSI model.
 870 The scheme is based on a Cauchy’s θ -like method with Nitsche approach to impose the coupling

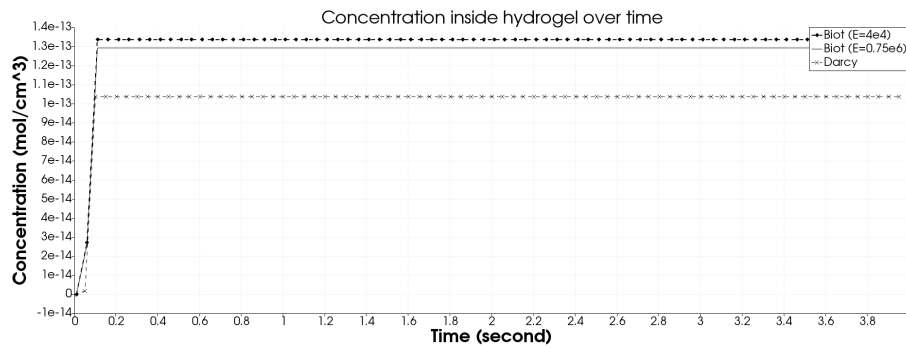


FIG. 20. The curves show oxygen concentration over time for three different hydrogels with three different elasticity moduli: alginate hydrogel with Young's modulus $E = 4 \times 10^4$ Pascals, alginate with $E = 0.75 \times 10^6$ Pa, and a very stiff scaffold made of Polycaprolactone (PCL) with $E = 1.3 \times 10^8$ Pa. We see a significant increase in oxygen concentration for the most elastic alginate hydrogels with $E = 4 \times 10^4$ Pa and $E = 0.75 \times 10^6$ Pa over the stiff PLC with $E = 1.3 \times 10^8$ Pa.

871 conditions. We prove rigorously that the resulting scheme is unconditionally stable when Nitsche's
 872 parameter is larger than a certain quantity, and we show that the method is second-order accurate
 873 in time using the method of manufactured solutions. At the micro-scale, Smoothed Particle
 874 Hydrodynamics (SPH) simulations are used to simulate local hydraulic permeability for a given
 875 hydrogel macro-architecture, from where hydrogel-specific macro-scale permeability tensor is
 876 derived. To avoid expensive 3D SPH simulations for each new hydrogel structure, Endoder-
 877 Decoder Neural Networks are used for parameter estimation of the macro-scale permeability
 878 tensor based on the micro-scale hydrogel architecture.

879 Our computational results show that:

- 880 1. Oxygen concentration and filtration flow through hydrogel scaffolds are significantly
 881 affected by the position and number of the ultrafiltrate outlets. The ultrafiltrate outlets
 882 should be (equi)distributed to uniformly cover the entire array of cell scaffolds.
- 883 2. Hydrogel elasticity significantly affects oxygen concentration and filtration flow through
 884 scaffolds. Highly elastic scaffolds have a higher capacity for oxygen transfer.
- 885 3. Oxygen concentration is largest near the flow inlet into the scaffold, and near the drilled
 886 ultrafiltrate channels.

887 The mathematical and computational approaches developed in this work provide a bench-
 888 mark tool for computational analysis of not only iBAP, but also, more generally, of cell encap-
 889 sulation strategies used in the design of devices for cell therapy and bio-artificial organs.

890 Extensions of this work include geometric optimization of ultrafiltrate channels' distribution
 891 maximizing oxygen concentration within a given hydrogel, the development of different, more
 892 efficient, numerical methods to simulate the micro-scale ultrafiltrate flow, and inclusion of an
 893 advection-reaction-diffusion model for insulin concentration.

894 **Acknowledgments.** This work has been supported in part by the National Science Founda-
 895 tion (NSF) under grants DMS-2011319 and DMS-1853340 (Čanić and Wang), and DMS-1912908
 896 and DCSD-934300 (Bukač), and by JDRF Encapsulation Consortium under grant 3-SRA-015-
 897 37-Q-R (Roy and Blaha) and the National Institutes of Health (NIH) under grants U01EB025136
 898 and R44DK104299 (Roy and Blaha). Partial postdoctoral support for Wang from the University
 899 of California, Berkeley is also acknowledged. The support from the University of California,
 900 Berkeley's Miller Institute is also acknowledged since a part of this work was done during Čanić's
 901 Miller Institute Professorship in 2021-2022.

902

REFERENCES

- 903 [1] M. ALONZO, S. KUMAR, S. ALLEN, M. DELGADO, F. ALVAREZ-PRIMO, L. SUGGS, AND B. JODDAR, *Hydrogel*
 904 *scaffolds with elasticity-mimicking embryonic substrates promote cardiac cellular network formation*,
 905 *Prog Biomater.*, 9 (2020), pp. 125–137.
- 906 [2] I. AMBARTSUMYAN, V. J. ERVIN, T. NGUYEN, AND I. YOTOV, *A nonlinear stokes–biot model for the interac-*
 907 *tion of a non-newtonian fluid with poroelastic media*, *ESAIM: Mathematical Modelling and Numerical*
 908 *Analysis*, 53 (2019), pp. 1915–1955.
- 909 [3] I. AMBARTSUMYAN, E. KHATTATOV, I. YOTOV, AND P. ZUNINO, *A Lagrange multiplier method for a Stokes–*
 910 *biot fluid-poroelastic structure interaction model*, *Numerische Mathematik*, (2018), pp. 1–41.
- 911 [4] M. BAYMANI, *Artificial neural network method for solving the Navier-Stokes equations*, *Neural Comput and*
 912 *Applic*, 26 (2015), pp. 765–773.
- 913 [5] D. BEARD AND J. BASSINGTHWAIGHTE, *Modeling advection and diffusion of oxygen in complex vascular*
 914 *networks*, *Annals of Biomedical Engineering*, 29 (2001), pp. 298–310.
- 915 [6] E. BERGKAMP, C. VERHOOSSEL, J. REMMERS, AND D. SMEULDERS, *A staggered finite element procedure*
 916 *for the coupled stokes-biot system with fluid entry resistance*, *Computational Geosciences*, 24 (2020),
 917 pp. 1497–1522.
- 918 [7] P. BUCHWALD, *FEM-based oxygen consumption and cell viability models for avascular pancreatic islets*,
 919 *Theoretical Biology and Medical Modelling*, 6 (2009), pp. 5–18.
- 920 [8] P. BUCHWALD, *A local glucose-and oxygen concentration-based insulin secretion model for pancreatic islets*,
 921 *Theoretical Biology and Medical Modelling*, 8 (2011), p. <http://www.tbiomed.com/content/8/1/20>.
- 922 [9] P. BUCHWALD AND S. R. CECHIN, *Glucose-stimulated insulin secretion in isolated pancreatic islets: multi-*
 923 *physics fem model calculations compared to results of perfusion experiments with human islets*, *Journal*
 924 *of Biomedical Science and Engineering*, 6 (2013), p. 2635.
- 925 [10] P. BUCHWALD, S. R. CECHIN, J. D. WEAVER, AND C. L. STABLER, *Experimental evaluation and computa-*
 926 *tional modeling of the effects of encapsulation on the time-profile of glucose-stimulated insulin release*
 927 *of pancreatic islets*, *Biomedical engineering online*, 14 (2015), pp. 1–14.
- 928 [11] P. BUCHWALD, A. TAMAYO-GARCIA, V. MANZOLI, A. A. TOMEI, AND C. L. STABLER, *Glucose-stimulated*
 929 *insulin release: parallel perfusion studies of free and hydrogel encapsulated human pancreatic islets*,
 930 *Biotechnology and bioengineering*, 115 (2018), pp. 232–245.
- 931 [12] M. BUKAC, I. YOTOV, R. ZAKERZADEH, AND P. ZUNINO, *Partitioning strategies for the interaction of a*
 932 *fluid with a poroelastic material based on a Nitsche’s coupling approach*, *Comput. Methods Appl. Mech.*
 933 *Engrg.*, 292 (2015), pp. 138–170, <https://doi.org/10.1016/j.cma.2014.10.047>, <https://doi.org/10.1016/j.cma.2014.10.047>.
- 934 [13] M. BUKAC, I. YOTOV, AND P. ZUNINO, *An operator splitting approach for the interaction between a fluid*
 935 *and a multilayered poroelastic structure*, *Numer. Methods Partial Differential Equations*, 31 (2015),
 936 pp. 1054–1100, <https://doi.org/10.1002/num.21936>, <https://doi.org/10.1002/num.21936>.
- 937 [14] J. BURKARDT AND C. TRENCHIA, *Refactorization of the midpoint rule*, *Applied Mathematics Letters*,
 938 107 (2020), p. 106438, <https://doi.org/10.1016/j.aml.2020.106438>, <https://doi-org.pitt.idm.oclc.org/10.1016/j.aml.2020.106438>.
- 939 [15] A. CEMELIOGLU AND P. CHIDYAGWAI, *Numerical analysis of the coupling of free fluid with a poroelastic*
 940 *material*, *Numerical Methods for Partial Differential Equations*, 36 (2020), pp. 463–494.
- 941 [16] S. CHEN, R. HUANG, AND K. RAVI-CHANDAR, *Linear and nonlinear poroelastic analysis of swelling and*
 942 *drying behavior of gelatin-based hydrogels*, *International Journal of Solids and Structures*, 195 (2020),
 943 pp. 43–56.
- 944 [17] J. COLLINS, A. RUDENSKI, J. GIBSON, L. HOWARD, AND R. O’DRISCOLL, *Relating oxygen partial pressure,*
 945 *saturation and content: the haemoglobin-oxygen dissociation curve*, *Breathe (Sheffield, England)*, 11
 946 (2015), pp. 194–201.
- 947 [18] T. DESAI AND L. SHEA, *Advances in islet encapsulation technologies*, *Nature Reviews (Drug Discovery)*, 16
 948 (2017), pp. 338–351.
- 949 [19] M. ETZOLD, P. LINDEN, AND M. WORSTER, *Transpiration through hydrogels*, *Journal of Fluid Mechanics*,
 950 925 (2021), pp. A8–1 – A8–31.
- 951 [20] FENICS, *Open source software developed by a global community of scientists and software developers*,
 952 <https://fenicsproject.org/>.
- 953 [21] S. A. FERNANDEZ, K. S. CHAMPION, L. DANIELCZAK, M. GASPARRINI, S. PARASKEVAS, R. L. LEASK, AND
 954 C. A. HOESLI, *Engineering vascularized islet macroencapsulation devices: An in vitro platform to study*
 955 *oxygen transport in perfused immobilized pancreatic beta cell cultures*, *Frontiers in bioengineering and*
 956 *biotechnology*, 10 (2022).
- 957 [22] W. H. FISSELL, A. DUBNISHEVA, A. N. ELDRIDGE, A. FLEISCHMAN, A. L. ZYDNEY, AND S. ROY, *High-*
 958 *performance silicon nanopore hemofiltration membranes*, *Journal of Membrane Science*, 326 (2009),
 959 pp. 58–63.
- 960 [23] E. X. HAN, J. WANG, M. KURAL, B. JIANG, K. L. LEIBY, N. CHOWDHURY, G. TELLIDES, R. G. KIBBEY,

- 963 J. H. LAWSON, AND L. E. NIKLASON, *Development of a bioartificial vascular pancreas*, Journal of tissue
 964 engineering, 12 (2021), p. 20417314211027714.
- 965 [24] E. IRITANI, N. KATAGIRI, K. YAMAGUCHI, AND J.-H. CHO, *Compression-permeability properties of com-*
 966 *pressed bed of superabsorbent hydrogel particles*, Drying Technology, 24 (2006), pp. 1243–1249.
- 967 [25] W. JAGER AND A. MIKELIC, *On the boundary conditions at the contact interface between a porous medium*
 968 *and a free fluid*, Ann. Scuola Norm. Sup. Pisa Cl. Sci. (4), 23 (1996), pp. 403–465, [http://www.numdam.](http://www.numdam.org/item?id=ASNSP_1996_4_23_3_403_0)
 969 [org/item?id=ASNSP_1996_4_23_3_403_0](http://www.numdam.org/item?id=ASNSP_1996_4_23_3_403_0).
- 970 [26] W. JAGER AND A. MIKELIC, *On the interface boundary condition of Beavers, Joseph, and Saffman*, SIAM J.
 971 Appl. Math., 60 (2000), pp. 1111–1127, <https://doi.org/10.1137/S003613999833678X>, [https://doi.org/](https://doi.org/10.1137/S003613999833678X)
 972 [10.1137/S003613999833678X](https://doi.org/10.1137/S003613999833678X).
- 973 [27] D. KANANI, W. H. FISSELL, S. ROY, A. DUBNISHEVA, A. FLEISCHMAN, AND A. L. ZYDNEY, *Permeability-*
 974 *selectivity analysis for ultrafiltration: Effect of pore geometry*, J. Memb. Sci., 349 (2010), pp. 405–418.
- 975 [28] S. KIM, B. FEINBERG, R. KANT, B. CHUI, K. GOLDMAN, J. PARK, W. MOSES, C. BLAHA, Z. IQBAL,
 976 C. CHOW, N. WRIGHT, W. H. FISSELL, A. ZYDNEY, AND S. ROY, *Diffusive silicon nanopore membranes*
 977 *for hemodialysis applications*, PLOS One, 11 (2016), p. e0159526.
- 978 [29] T. LHIVAARA, L. KRKKINEN, J. M. J. HUTTUNEN, AND J. S. HESTHAVEN, *Deep convolutional neural networks*
 979 *for estimating porous material parameters with ultrasound tomography*, The Journal of the Acoustical
 980 Society of America, 143 (2018), pp. 1148–1158, <https://doi.org/10.1121/1.5024341>.
- 981 [30] A. MASUD AND T. HUGHES, *A stabilized mixed finite element method for Darcy flow*, Comput. Methods
 982 Appl. Mech. Engrg., 191 (2002), pp. 4341–4370.
- 983 [31] J. J. MONAGHAN., *Smoothed particle hydrodynamics.*, Annual Review of Astronomy and Astrophysics, 30
 984 (1992), pp. 543–574.
- 985 [32] J. J. MONAGHAN., *Simulating free surface flows with SPH.*, J. Comput. Phys., 110 (1994), pp. 399–406.
- 986 [33] J. P. MORRIS, P. J. FOX, AND Y. ZHU., *Modeling low Reynolds number incompressible flows using SPH.*,
 987 J. Comput. Phys., 136 (1997), pp. 214–226.
- 988 [34] M. RAISSI, A. YAZDANI, AND G. E. KARNIADAKIS, *Hidden fluid mechanics: A Navier-Stokes informed deep*
 989 *learning framework for assimilating flow visualization data*, ArXiv, abs/1808.04327 (2018).
- 990 [35] A. D. RAUCH, A.-T. VUONG, L. YOSHIHARA, AND W. A. WALL, *A coupled approach for fluid saturated*
 991 *poroelastic media and immersed solids for modeling cell-tissue interactions*, International Journal for
 992 Numerical Methods in Biomedical Engineering, 34 (2018), p. e3139.
- 993 [36] R. RUIZ-BAIER, M. TAFFETANI, H. D. WESTERMEYER, AND I. YOTOV, *The biot–stokes coupling using total*
 994 *pressure: Formulation, analysis and application to interfacial flow in the eye*, Computer Methods in
 995 Applied Mechanics and Engineering, 389 (2022), p. 114384.
- 996 [37] R. SHAHEEN, R. GURLIN, R. GOLOGORSKY, C. BLAHA, P. CARNESE, M. HEBROK, P. MUNNANGI, G. NAIR,
 997 AND S. ROY, *Superporous agarose scaffolds for encapsulation of adult human islets and human stem-*
 998 *cell-derived β cells for intravascular bioartificial pancreas applications*, J Biomed Mater Res, 109 (2021),
 999 pp. 2438–2448.
- 1000 [38] S. SONG, G. GAETANO FALEO, R. YEUNG, R. KANT, A. M. POSSELT, T. A. DESAI, Q. TANG, AND S. ROY,
 1001 *Silicon nanopore membrane (SNM) for islet encapsulation and immunoisolation under convective trans-*
 1002 *port*, Nature Scientific Reports, 6 (2016), pp. 1–9.
- 1003 [39] S. SONG, C. BLAHA, W. MOSES, J. PARK, N. WRIGHT, J. GROSZEK, W. FISSELL, S. VARTANIAN, A. M.
 1004 POSSELT, AND S. ROY, *An intravascular bioartificial pancreas device (iBAP) with silicon nanopore mem-*
 1005 *branes (SNM) for islet encapsulation under convective mass transport*, Lab Chip, 17 (2018), pp. 1778–
 1006 1792.
- 1007 [40] M. TAFFETANI, R. RUIZ-BAIER, AND S. WATERS, *Coupling stokes flow with inhomogeneous poroelasticity*,
 1008 The Quarterly Journal of Mechanics and Applied Mathematics, 74 (2021), pp. 411–439.
- 1009 [41] V. THOMEE, *Galerkin finite element methods for parabolic problems*, Springer series in computational math-
 1010 ematics., 25 (2006).
- 1011 [42] S. ČANIĆ, Y. WANG, AND M. BUKAČ, *A next-generation mathematical model for drug-eluting stents*, SIAM
 1012 Journal on Applied Mathematics, 81 (2021), pp. 1503–1529.
- 1013 [43] Y. WANG, S. CANIC, G. KOKOT, A. SNEZHKO, AND I. ARANSON., *Quantifying the role of hydrodynamic*
 1014 *interactions on the onset of collective states in ensembles of magnetic colloidal spinners and rollers.*,
 1015 Physical Review Fluids, 4 (2019), p. 013701.
- 1016 [44] J. WEN AND Y. HE, *A strongly conservative finite element method for the coupled stokes–biot model*, Com-
 1017 puters & Mathematics with Applications, 80 (2020), pp. 1421–1442.
- 1018 [45] J. WEN, J. SU, Y. HE, AND H. CHEN, *Discontinuous galerkin method for the coupled stokes-biot model*,
 1019 Numerical Methods for Partial Differential Equations, 37 (2021), pp. 383–405.
- 1020 [46] J. YOON, S. CAI, Z. SUO, AND R. C. HAYWARD, *Poroelastic swelling kinetics of thin hydrogel layers: com-*
 1021 *parison of theory and experiment*, Soft Matter, 6 (2010), pp. 6004–6012.